MNRAS **000**, 1–21 (2015) Preprint 23 February 2016 Compiled using MNRAS LATEX style file v3.0

Super- and sub-Eddington accreting massive black holes: A comparison of slim and thin accretion discs through study of the spectral energy distribution.

N. Castelló-Mor[1⋆], H. Netzer[1] and S. Kaspi[1,2]
[1] *School of Physics and Astronomy, Tel Aviv University, Tel Aviv 69978, Israel*
[2] *Wise Observatory, School of Physics and Astronomy, Tel Aviv University, Tel Aviv 69978, Israel*

arXiv:1601.07177v3 [astro-ph.GA] 21 Feb 2016

Accepted XXX. Received YYY; in original form ZZZ

ABSTRACT

We employ optical and UV observations to present SEDs for two reverberation-mapped samples of super-Eddington and sub-Eddington AGN with similar luminosity distributions. The samples are fitted with accretion disc models in order to look for SED differences that depend on the Eddington ratio. The fitting takes into account measured BH mass and accretion rates, BH spin and intrinsic reddening of the sources. All objects in both groups can be fitted by thin AD models over the range 0.2-1 μm with reddening as a free parameter. The intrinsic reddening required to fit the data are relatively small, $E(B-V) \leq 0.2$ mag, except for one source. Super-Eddington AGN seem to require more reddening. The distribution of $E(B-V)$ is similar to what is observed in larger AGN samples. The best fit disc models recover very well the BH mass and accretion for the two groups. However, the SEDs are very different, with super-Eddington sources requiring much more luminous far-UV continuum. The exact amount depends on the possible saturation of the UV radiation in slim discs. In particular, we derive for the super-Eddington sources a typical bolometric correction at 5100Å of 60–150 compared with a median of ∼20 for the sub-Eddington AGN. The measured torus luminosity relative to λL_λ(5100Å) are similar in both groups. The α_{OX} distribution is similar too. However, we find extremely small torus covering factors for super-Eddington sources, an order of magnitude smaller than those of sub-Eddington AGN. The small differences between the groups regarding the spectral range 0.2-22 μm, and the significant differences related to the part of the SED that we cannot observe may be consistent with some slim disc models. An alternative explanation is that present day slim-disc models over-estimate the far UV luminosity of such objects by a large amount.

Key words: accretion,accretion discs – galaxies: nuclei – galaxies: Seyfert – galaxies: active

1 INTRODUCTION

Optically thick accretion flows in the vicinity of the central black hole (BH) are believed to be the main power-house of active galactic nuclei (AGN). The emitted radiation from such systems is determined by the BH mass (M_{BH}), BH spin ($a_\star$), and the mass accretion rate, $\dot{M}$. The accretion rate can be expressed in normalized units, or Eddington ratio, $\dot{m} = L_{\rm AGN}/L_{\rm Edd}$, where $L_{\rm AGN}$ is the bolometric luminosity of the system. Optically thick geometrically thin accretion discs (ADs) have been proposed to explain the observed spectral energy distribution (SED) of many AGN with low Eddington ratios ($L_{\rm AGN}/L_{\rm Edd} \leq 0.3$, Koratkar & Blaes 1999; Blaes et al. 2001; Shang et al. 2005; Davis et al. 2007; Davis & Laor 2011; Laor & Davis 2011; Jin et al. 2012; Slone & Netzer 2012; Netzer & Trakhtenbrot 2014; Capellupo et al. 2015). At higher accretion rates, the disc becomes "thick" or "slim" and the nature of the accretion changes dramatically with processes like photon trapping and advection becoming important (Abramowicz et al. 1988; Sądowski et al. 2014, see review by Wang et al. 2014b). Slim ADs are thought to have SEDs that are different from thin ADs, with an energy cut-off that extends to higher energies and a strong anisotropy of the emitted radiation. We follow Wang et al. (2014a) and coin such objects "Super-Eddington Accreting Massive Black Holes" (SEAMBHs).

⋆ E-mail: nuria@wise.tau.ac.il (TAU)

© 2015 The Authors

The radiation efficiency of thin ADs around BHs, η, defined by $L_{\rm AGN} = \eta \dot{M}_{BH} c^2$, is obtained from the standard AD theory (e.g. Shakura & Sunyaev 1973; Thorne 1974). η depends on the location of the innermost stable circular orbit (ISCO) which in turn depends on the BH spin. For maximally rotating BHs, with spin parameter $a_\star = 0.998$, $\eta = 0.32$ and for retrograde discs, with $a_\star = -1$, $\eta = 0.038$. This is not the case for slim ADs that are not well understood. In such cases, there is an ill-defined radiation efficiency that may not depend on the BH spin and is suggested to be considerably smaller than the corresponding thin AD efficiency due to the so-called "photon trapping". The issue is particularly important for very high accretion rates where the theoretical models suggest that the emitted radiation follows an expression of the type (Mineshige et al. 2000)

$$L_{\rm AGN} \approx 3 \times 10^{38} \left[1 + \ln \dot{\mathcal{M}}/\dot{\mathcal{M}}_{crit}\right] M_{BH} \quad (1)$$

where $\dot{\mathcal{M}}$ is the dimensionless accretion rate defined as $\dot{m} = \eta \dot{\mathcal{M}}$ and $\dot{\mathcal{M}}_{crit} \approx 20$ (Du et al. 2015). Such theoretical approximations are yet to be confirmed by numerical simulations. For example, the recent numerical simulations of such objects by Sądowski & Narayan (2015) suggest a relatively small drop in efficiency up to extremely high accretion rates. Finally, all AGN are known to be powerful X-ray sources with $L_{2-10\,\rm keV}$ luminosity that, in most observed cases, is considerably below the integrated optical-UV luminosity (e.g. Marconi et al. 2004; Steffen et al. 2006; Vasudevan & Fabian 2007, 2009; Grupe et al. 2010; Marchese et al. 2012). The dimension and variability of the X-ray source suggest that it is intimately related to the accretion process, thus the emitted X-ray radiation is most probably drawn from the accretion process itself. This must be taken into account when comparing the radiation efficiencies of thin and slim ADs.

The observed optical-UV SEDs of some AGN resemble the prediction of the thin AD model. In particular, they show a prominent bump in the optical-ultraviolet, the *Big Blue Bump* (BBB), which peaks at a BH-mass dependent frequency and declines at higher energies. Unfortunately, the comparison with theoretical AD SEDs has been hampered by the lack of simultaneous observations of these highly variable sources, and the limited wavelength range of most observations. Another source of uncertainty is intrinsic reddening due to dust in the host galaxy of the AGN. Because of this, many earlier studies failed to reach a conclusion regarding the origin of the observed SED with only marginal indications for a disc-like spectrum (see Koratkar & Blaes 1999; Davis et al. 2007). Moreover, an empirical SED made of a broken power-law with slopes $-0.5 < \alpha < 1.5$, where $F_\nu \propto \nu^{-\alpha}$, have been shown to give better fits to many observed, limited wavelength spectra (Zheng et al. 1997).

The recent work of Capellupo et al. (2015) shed new light on this issue. The work is based on VLT/Xshooter observations of 39 type-I AGN with $z \approx 1.55$ and a large range of $L_{\rm AGN}$ and $\dot{m}$. They provide simultaneous information on the rest-frame wavelength range of 1100-9200Å which is large enough to test the AD model predictions. More than 90% of the sources in this sample are well fitted with a thin AD model. The fitting requires moderate intrinsic reddening in ∼30% of the sources with extinction in the range $0.1 < A_V < 0.5$ mag. This indicates that many earlier attempts to discover the unique spectral signature of thin ADs failed as a result of AGN variability and non-simultaneous data that cover only a limited wavelength range. All the sources in the Capellupo et al. (2015) sample are relatively low accretion rate systems with 90% of the sources in the range $10^{-2} < \dot{m} < 0.3$ and not a single source with $\dot{m} > 1$.

The most accurate information about $\dot{m}$ in type-I AGN is obtained for sources with directly measured BH mass through reverberation mapping (RM). Such information is now available for about 40 objects with $\dot{m} < 0.1$ (see Bentz et al. 2013) and for 15 objects with $\dot{m} > 0.1$ (Du et al. 2015, the objects we refer to as SEAMBHs). The comparison of the two groups suggests that for a given optical luminosity, the emissivity weighted radius of the broad line region (BLR) is considerably smaller in SEAMBHs with differences that can amount to a factor of ≈ 3. As explained in Wang et al. (2014a) and Du et al. (2015), this can be interpreted as a change in the nature of the power-house where the lower $\dot{m}$ systems are powered by thin ADs and the higher $\dot{m}$ objects by slim ADs.

There are several other well known difference between high and low $\dot{m}$ systems. The first is the nature of their X-ray continuum manifested by higher variability amplitude, steeper soft X-ray slope and larger α_{OX} (the slope connecting the flux at 2500Å and 2 keV) for the higher $\dot{m}$ objects. These differences have been studied, extensively, in numerous papers (Pogge 2000; Steffen et al. 2006; Gallo 2006), especially among lower luminosity AGN. Clear spectroscopic differences are also found at optical-UV wavelengths where, for a given monochromatic luminosity, the higher $\dot{m}$ sources show narrower broad emission lines and much stronger FeII lines. Such objects have been named "narrow line Seyfert 1 galaxies" (NLS1s). Their spectral differences are well characterized in the "eigen-vector 1" scheme (Sulentic et al. 2000).

The goal of the present work is to make a detailed comparison of the optical-UV SEDs of sub-Eddington and super-Eddington AGN. The number of accurately measured BH mass in SEAMBHs has reached a stage where such a comparison is feasible and can be used to test various models and scenarios related to the AGN power-house and the accretion process itself. In particular, we want to test whether thin and slim AD models reliably explain the observed optical-UV SED of such objects and the properties of their dusty tori, and test the differences, if any, between the two groups. An important aim of the present work is to improve the X-ray-to-optical SED measurements and hence the estimates of the bolometric luminosity of AGN in sources powered by thin or slim ADs. The pioneering study of Elvis et al. (1994) presented radio-to-X-ray SEDs for quasar, is restricted to bright X-ray sources and cover both the intrinsic AGN continuum and the processed torus emission. Unfortunately, the processed radiation is added to the intrinsic emission which results in double counting and too large bolometric correction factors. In later works, double counting was avoided, but intrinsic reddening and host galaxy contribution was not taken into account (see e.g. Marconi et al. 2004; Hopkins et al. 2004; Richards et al. 2006; Vasudevan & Fabian 2007). This affects the bolometric luminosity measurements, underestimating its value. More recent works (Brocksopp et al. 2006; Vasudevan & Fabian 2009, Vasudevan et al. 2009 hereafter V09, Jin et al. 2012, among others), presented optical-to-X-ray SED emphasizing interesting trends between SED

signature and Eddington ratio. However, most samples were restricted to low accretion rate AGN. In particular, there was a lack of super-Eddington sources with reliable, RM-based BH mass estimates since such objects were not known at the time.

The sample of AGN presented here is restricted to those AGN which are bright enough in the optical/UV and all have direct mass measurements. There are 29 objects selected by their spectroscopic properties with 16 of those showing extremely high accretion rates (referred to as super-Eddington AGN). This makes our approach different than all previous studies. From all previous studies, the work of V09 is the one most similar to ours. It takes into account reddening and host galaxy corrections in the optical/UV, but focus on low accretion rate sources and does not discuss the torus properties. Below we show the similarity between V09 and our study regarding sub-Eddington AGN, and the missing information about the torus, and make detailed comparison with the new group of super-Eddington sources. The most recent works of Marchese et al. (2012) and Fanali et al. (2013) are other attempts to correlate accretion disc and X-ray properties of luminous AGN. There are several fundamental differences between these papers and the present work. First, the BH mass estimate is based on single-epoch (virial) method. Second, the accretion disc model is not a fit to individual SEDs but rather the same model for all sources with an assumed stationary BH but an efficiency η of 0.1 which is more appropriate to rotating BH. Third, and most important, the three bands used for the estimate bolometric luminosity (X-ray XMM-Newton, UV GALEX and optical SDSS) are not obtained simultaneously which, as we show below, introduces an uncertainty which is impossible to estimate. Because of these differences we do not attempt to compare the results obtained in these papers to the one presented below. Recently, Jin et al. (2016) presented a new result for a super-Eddington source RX J1140.1+0307, where upper limit on the BH mass was obtained through RM (the upper limit is on the $H\beta$ time lag). Jin et al. (2016) present several SED fits based on accretion disc models using non-simultaneous data. There are also difficulties in host galaxy subtraction and reddening correction. Jin et al. (2016) found that the best-fit SED overestimate the mass of the black hole by an order of magnitude relative to the RM results. Because of these and the fact that the source is in the lowest black hole mass regime we do not attempt to compare their results to the ones presented here.

The structure of the paper is as follows. In Section 2 we describe the sample selection and the observational data. In section 3 we describe the intrinsic disc SED that we use and the fitting procedure is presented in section 4. The principal results of the thin AD modelling and some additional spectral properties are presented in Section 5. Finally, in Section 6, we summarize our main conclusions from this work. Throughout this paper we assume a ΛCDM cosmology with $\Omega_\Lambda = 0.7$, $\Omega_m = 0.3$, and $H_0 = 70$ km/s/Mpc.

2 SAMPLE SELECTION

The goal of this work is to compare various properties of high Eddington ratio AGN with RM-measured BH mass with a similar group of low Eddington ratio AGN. Our high Eddington ratio sample consists of 16 radio-quiet AGN that are basically all the potential SEAMBH candidates listed in the Du et al. (2015) sample. The BLR sizes of 13 of the sources were measured in a two-year RM-campaign on the Lijiang 2.4m telescope by the "SEAMBH Collaboration". The objects were selected by their spectroscopic properties. They are all NLS1s with suspected high Eddington ratio, $\dot{m}$. The selection assumes a conservative method to estimate the normalized accretion rate $\dot{\mathcal{M}} \geq 3$. The value was chosen to make sure that $\dot{m}$ for the lowest efficiency discs (those with spin -1 and $\eta = 0.038$) exceeds 0.1 (Du et al. 2014; Wang et al. 2014a; Du et al. 2015). Three additional SEAMBHs candidates, PG 2130+099, PG 0844+349 and Mrk 110, with similar properties, were selected from the general catalogue of ~ 50 RM-AGN. As of early 2015, these are the best candidates for being super-Eddington accretors. We coin this sample the "super-Eddington group".

We have also selected a control sample of 13 type-I AGN from the general group of ∼50 RM objects with a much smaller Eddington ratio (defined in the same way) and $\dot{\mathcal{M}} < 3$. This group, named as super-Eddington, was selected to overlap in optical luminosity, defined as λL_λ at the rest-frame wavelength 5100Å, the luminosity of the super-Eddington group. The luminosity distributions of the two groups are compared in Figure 1. Although the Kolmogorov-Smirnov test can not reject the hypothesis that both luminosity distributions are drawn from the same distribution, there is a factor two on its average rest-frame 5100Å luminosity which can not be improved due to the limited RM-AGN sample (10^{44} erg/s and $4.8{\times}10^{44}$ erg/s for super-Eddington and sub-Eddington groups, respectively). The redshift distribution of the sub-Eddington group is quite similar to the range covered by our super-Eddington objects. The median redshifts are 0.054 and 0.031 for the super-Eddington and the sub-Eddington samples, respectively. Figure 1 also shows the distribution of the virial BH mass in the two samples. Due to the selection method which is based on source luminosity, the typical BH mass in the control sample is much larger.

2.1 Photometric and Spectroscopic Data

We have collected optical-UV photometric and spectroscopic data from various surveys and data bases. The data are used to define and separate stellar from non-stellar sources of continuum radiation and to constrain the properties of the SEDs of all sources. The optical spectrum of 17 RM objects were taken from the Sloan Digital Sky Survey (SDSS) DR10. For the remaining 12 sources, we used a mean optical spectrum from previous reverberation mapping campaigns. From the AGN Watch database[1] we selected the mean spectrum of Mrk 279, Mrk 509, NGC 7469 and Fairall 9. The mean optical spectrum of Mrk 79 and Mrk 817 were given by Peterson M.B. (private communication, Peterson et al. 1998). The mean optical spectrum of the Palomar Green (PG) quasars (PG 2130+099, PG 0844+349, and PG 1617+175) were

[1] The AGN Watch is a consortium of astronomers who have studied the inner structure of AGN through continuum and emission-line variability. See http://www.astronomy.ohio-state.edu/∼agnwatch/

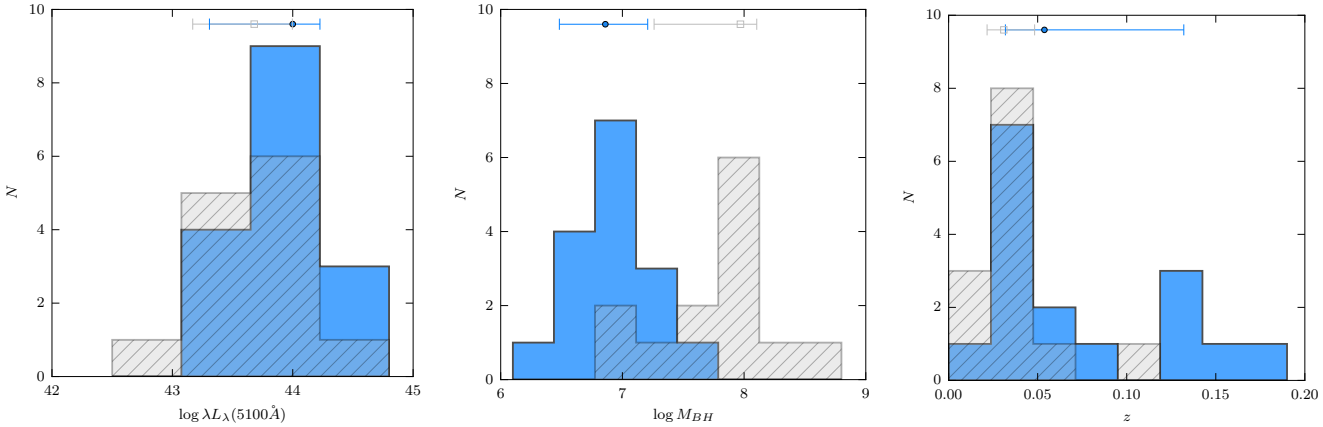

Figure 1. *From left to right*: Distributions of $\log \lambda L_\lambda(5100\text{Å})$, virial black hole mass, and redshift for both samples. Filled (blue) histogram represents super-Eddington AGN and hatched (grey) histogram sub-Eddington AGN. The point with error bars on the top of each panel is the median and the 16^{th} and 84^{th} percentiles for each group.

taken from Kaspi et al. (2000). Finally, the mean optical spectrum of Mrk 486, Mrk 335 and Mrk 1044 are those published by the "SEAMBH Collaboration" (Du et al. 2014). All objects in our sample, except for Mrk 79 and PG 1617+175, have high quality optical spectra with broad optical wavelength range.

All objects in this work, except for Mrk 486, PG 0844+349 and SDSS J080101.14+184840.7, have NUV and FUV photometry (2306Å and 1551Å, respectively) obtained by the NASA Galaxy Evolution Explorer (GALEX). The GALEX fluxes were collected from the online database and all image were inspected visually. We found 23 objects with observations in the all-sky imaging survey (AIS). In addition, three objects (Mrk 1044, IRAS 04416+1215, Mrk 590) are also included in the medium imaging survey (MIS). No discrepancy was found between both observations (a difference between AIS and MIS photometry less than 0.15 magnitudes in both GALEX bands). Three out of these 23 objects have been detected in different surveys: PG 2130+099 was found in the MIS, while NGC 5548 and PG 1229+204 were selected from the Guest Investigator (GI) program. For 17 objects we also assembled optical/UV photometry from the *XMM-Newton* Optical Monitor (OM): V 5430Å, B 4500Å, U 3440Å, UVW1 2910Å, UVM2 2310Å and UVW2 2120Å. From visually inspection of the available Hubble Space Telescope (HST) data we cannot extend our dataset into the extreme UV because of variability, i.e. there is at least a factor 2 on flux between the HST spectrum and the selected optical/UV dataset.

Summarizing, of our 29 sources we have optical spectra in conjunction with GALEX photometry for 26 sources and 16 sources which, in addition to these data, also have XMM-OM photometry, and in 8 cases simultaneous optical/UV photometry. A detailed list of all the observations is given in Table 1.

3 OBSERVED AND INTRINSIC SEDS

A central goal of the present work is to compare the multi-wavelength SEDs of super-Eddington and sub-Eddington AGN. For this we need to correct for non-simultaneous observations, to subtract the stellar and emission line contributions, and to consider the possibility of intrinsic reddening of the sources. As for Galactic interstellar reddening, this is done assuming the Cardelli et al. (1989) extinction law using the Galactic extinction colour excess $E(B-V)$ obtained from the NASA/IPAC Infrared Science Archive[2].

3.1 Long term optical-UV variability

The presence of variability in the optical/UV continuum of all the sources in our sample is well documented. Whilst we can expect variability of order a few per cent in the optical-UV continuum on short-time of days to a week, much larger factors are expected on time scales of months and years. For example, Santos-Lleó et al. (1997) found a factor of ∼2 for Fairall 9 in the optical continuum flux over a three month period and even larger factors have been found for NGC 5548 (a factor of ∼7 over a seven years period, Peterson et al. 1999). Therefore variability is the main challenge for the work presented here.

The information that is available for most sources is a combination of optical spectroscopy and GALEX photometry. Most of these data are not simultaneous. In order to avoid as much as possible the non-simultaneity, and to complete the UV GALEX information, we used data obtained by the *XMM-Newton* Optical Monitor (OM). OM photometry was available for 17 out of 29 objects and contemporaneous optical/UV observations (at least 5 simultaneous OM points) for only 6 sources (see Table 1). These contemporaneous optical/UV observations provide reliable constraints on the source SEDs and help to reduce the fitting uncertainty (see Appendix B).

The heterogeneity of our optical/UV datasets dictate a somewhat different procedure for each of the fitted sources. Three different procedures were used: I) a simultaneous and non-simultaneous SED were fitted in order to quantify the non-contemporaneous SED shape; II) when simultaneous

[2] http://irsa.ipac.caltech.edu/applications/DUST/

Table 1. Optical and UV observations used to model the SED of super-Eddington (upper block) and sub-Eddington AGN (lower block).

		Optical Spectrum		GALEX		*XMM-Newton* OM	
Object	$E(B-V)_{\rm Gal}$	survey	date	survey	date	XMMOM	date
Mrk 142	0.016	SDSS DR10	2003-03-09	AIS	2004-01-22		
Mrk 335	0.035	SEAMBH Collaboration	2012 Oct – 2013 Feb	AIS	2007-04-02	J000619.5+201211	2007-07-10
Mrk 382	0.048	SDSS DR10	2001-10-19	AIS	2007-01-21	J075525.3+391110	2011-11-02
Mrk 486	0.015	SEAMBH Collaboration	2013 Mar – 2013 Jul				
Mrk 493	0.025	SDSS DR10	2004-05-16	AIS	2007-05-26		
Mrk 1044	0.033	SEAMBH Collaboration	2012 Oct – 2013 Feb	MIS	2008-10-11		
IRAS 04416+1215	0.436	SDSS DR10	2006-12-17	MIS	2008-12-17		
IRAS F12397+3333	0.019	SDSS DR10	2005-03-02	AIS	2004-04-15	J124210.6+331702	2005-06-20
SDSS J075101.42+291419.1	0.042	SDSS DR10	2002-12-28	AIS	2007-01-18		
SDSS J080101.41+184840.7	0.032	SDSS DR10	2004-11-10				
SDSS J081441.91+212918.5	0.039	SDSS DR10	2004-11-18	AIS	2006-01-27		
SDSS J081456.10+532533.5	0.032	SDSS DR10	2004-10-19	AIS	2004-01-13		
SDSS J093922.89+370943.9	0.014	SDSS DR10	2003-12-23	AIS	2005-08-12	J093922.9+370945	2006-11-01
PG2130+099	0.044	Kaspi et al. (2000)	1991 Aug – 1997 Oct	MIS	2009-08-22	J213227.8+100819	2003-05-16
PG0844+349	0.037	Kaspi et al. (2000)	1991 Aug – 1997 Oct			J084742.4+344504	2009-05-03
Mrk110	0.012	SDSS DR10	2001-12-09	AIS	2007-01-23	J092512.9+521711	2004-11-15
Mrk 79	0.071	Peterson et al. (1998)	1983 – 1985	AIS	2007-01-20	J074232.8+494835	2008-04-26
Mrk 279	0.016	AGN Watch	1996 Dec – 1997 Jan	AIS	2004-01-25	J135303.5+691830	2005-11-19
Mrk 290	0.014	SDSS DR10	2002-03-14	AIS	2005-10-22	J153552.3+575409	2006-05-04
Mrk 509	0.057	AGN Watch	1988 Sep – 1993 Dec	AIS	2007-02-09	J204409.7-104324	2009-11-14
Mrk 590	0.037	SDSS DR10	2003-01-08	MIS	2008-10-23		
Mrk 817	0.007	Peterson et al. (1998)	1983 – 1985	AIS	2007-02-21		
Mrk 1511	0.041	SDSS DR10	2007-04-17	AIS	2007-04-17	J153118.1+072729	2012-02-23
NGC 5548	0.020	SDSS DR10	2006-05-04	GII	2006-10-30	J141759.5+250813	2013-07-29
NGC 7469	0.068	AGN Watch	1996 Jun – 1996 Jul	AIS	2007-03-22	J230315.6+085226	2004-11-30
PG 1229+204	0.027	SDSS DR10	2008-01-16	GII	2007-05-22	J123203.7+200929	2005-07-09
PG 1617+175	0.042	Kaspi et al. (2000)	1991 Aug – 1997 Oct	AIS	2006-06-14		
Fairall9	0.025	AGN Watch	1994 May – 1995 Jan	AIS	2007-08-17	J012345.7-584820	2013-12-19
MCG+06-26-012	0.019	SDSS DR10	2005-03-31	AIS	2007-03-22		

dataset was not possible, both GALEX and OM photometry in conjunction with the optical spectrum were fitted as long as there is no signs of variability, i.e. all segments of the fitted continuum join smoothly; III) for those sources without *XMM-Newton* OM observations we fitted the non-simultaneous optical-GALEX SED assuming they were observed at a similar flux epoch. Comments on individual sources are given in Appendix B. This general procedure works well in all the objects discussed in the present paper although non-simultaneity is still the main limiting factor.

3.2 Host Galaxy Contribution

The optical/UV emission may be contaminated by starlight from the host galaxy. The relative contribution depends on the aperture size, AGN luminosity, and the stellar population in the host. Thus careful galaxy subtraction is necessary if we are to determine the SED shape. Such corrections are often made by subtracting galaxy bulge template spectra. Star formation in the central part must also be considered since the host of many AGN are star formation galaxies (e.g. Sani et al. 2010).

There are three methods that can be used to correct the observed spectra for host-galaxy contamination. The first is a direct subtraction of the stellar light measured from HST images. Such data are available for 25 of the sources (Peterson et al. 1998; Bentz et al. 2009; Du et al. 2014; Wang et al. 2014a). Published galaxy light profiles were used in these cases and normalized to the aperture in question. This correction is normally small (20-70%) for the 3″ SDSS fiber and considerably larger for the 6″ aperture of the optical OM filter. The second method makes use of empirical expressions derived by Shen et al. (2011) and Elvis et al. (2012). The uncertainty here is much larger because of the considerable range in host properties. Finally, one can use the fact that the broad Hβ lines show no Baldwin effect (Dietrich et al. 2002). This means that the observed equivalent width of the line, EW(Hβ), can be used to derive the fraction of the non-AGN light entering the aperture at 4861Å. Du et al. (2015) show the distributions of EW(Hβ) in low Eddington ratio AGN and in SEAMBHs. The two differ by a considerable amount with medians that are (122 ± 44)Å and (89 ± 31)Å, respectively. For those sources without HST observations,we prefer the use of this method over the expressions given by Shen et al. (2011). The main concern is how to treat the five objects without HST observations.

The subtraction procedure starts with an estimate of the non-AGN flux at 4861Å followed by a subtraction of a single simple stellar model spectrum which is scaled to this flux. A nominal 20% uncertainty on this flux was adopted due to a combination of the host-galaxy modelling and the uncertainties on the emission line fluxes. The SDSS fibers include only the innermost few kpc of the host, hence we chose a quiescent galaxy model from the evolutionary spec-

tral library of Charlot & Bruzual (1991). For 15 out of 29 objects, the instantaneous-burst model with an age of 11 Gyr and solar metallicity (Z=0.02) provided sufficiently good fit to the stellar spectrum. For the remaining 14 objects, this template gives a "flux excess" at the longest observed wavelengths. A template with 11 Gyr and Z=0.05 provides better fit to such spectra and was adopted in these cases. We also experimented with adding younger stellar population components but did not find significant improvements over the old population templates.

The difference on aperture between the SDSS fibres (3″) and the OM broadband filters (12″ and 35″ diameter for the optical and UV filter, respectively) prevent us from using the estimated host-galaxy contribution to the optical spectrum to subtract the star-light from the OM photometric data. For the OM photometric dataset, the host galaxy emission was modeled by adopting the published galaxy-light radial profiles (Bentz et al. 2009) which were integrated over the specific OM aperture to estimate the host-galaxy contribution to the total observed flux.

3.3 Emission line Contributions

The wavelength range for the photometry are wide enough that the underlying nuclear continuum might be contaminated by broad and narrow emission lines, i.e. Balmer lines, C IV, Mg II, Fe II, as well as the Balmer continuum.

In order to exclude the underlying continuum, we used the composite quasar spectrum of Vanden Berk et al. (2001) to estimate the emission line fraction for each photometric waveband. We assumed only the emitted flux in the spectral window over which the effective transmission is greater than 10% of the peak effective transmission: FUV 1343–1786Å, NUV 1771–2831Å, UVW2 1805–2454Å, UVM2 1970–2675Å, UVW1 2410–3565Å, U 3030–3890Å, B 3815–4910Å and V 5020–5870Å. For comparison, at redshift $z = 0.06$, which is the mean of our sample, the contributions from the emission line regions at each photometric window are 5%, 11.9%, 9.4%, 13.0%, 23.4%, 24.6%, 15.9% and 24.9% for FUV, NUV, UVW2, UVM2, UVW1, U, B and V, respectively. Since line variations follow continuum variations (albeit with somewhat different lags), we do not expect large fluctuations in these fractions.

3.4 Intrinsic reddening

Intrinsic extinction in AGN can be significant which can make it an important factor when determining the SED of the optical/UV continuum. Previous studies (Lusso et al. 2013; Capellupo et al. 2015; Collinson et al. 2015, Mejia-Restrepo et al. 2015 (submitted), and references therein) found a range of properties with most AGN showing little dust attenuation, i.e. $E(B-V)$<0.1, independent of the reddening law. Such reddening does not affect much the optical fluxes, but its effect on the UV part of the spectrum is significantly larger. Not accounting for this effect will result in fitting the wrong accretion disc models and the miss-calculation of source luminosity and accretion rate.

Extinction curves which are commonly used in AGN studies include: Milky Way-like extinction with its known broad bump at ∼2175Å, Small Magellanic Cloud-type (SMC) curves, a simple power-law extinction, or a combination of a power law with a flatter curve in the far-UV (Gaskell et al. 2004). Several earlier works (Hopkins et al. 2004; Glikman et al. 2012) claimed that the typical bump at 2175Å of the MW-like extinction curve is not observed in AGN spectra. Recent, higher quality spectra and more carefully fitted SEDs by Capellupo et al. (2015) clearly show this bump in some of the spectra.

Since the wavelength dependence of the extinction is unknown, a priori, we experimented with three possibilities: I) the Cardelli et al. (1989) as a MW-like curve with $R_V = 3.1$, II) a simple power-law $A(\lambda) = A_0\lambda^{-1}$, and III) the SMC extinction curve as given in Gordon et al. (2003). According to the wavelength dependence of the extinction curve, the intrinsic reddening will be larger for the SMC curve than for the MW. The most consistent approach is to add this extinction as an additional parameter in the SED modelling analysis. Clearly, if extinction is important, the intrinsic underlying continuum shape will depend significantly on the form of the reddening curve. As a practical point we note that the extremely broad GALEX bands do not allow us to take into account spectral features like the 2175Å absorption and weaker ISM lines and we only treat the total observed flux in these bands.

4 SED MODEL FITTING

4.1 Accretion disc models

In this work, we use the numerical code described in Slone & Netzer (2012) to calculate thin AD spectra. The calculations assume a Shakura & Sunyaev (1973) disc with a variable viscosity parameter (chosen in this paper to be $\alpha = 0.1$). As in all models of this type (see Sec. 1), the spin-dependent ISCO determines the mass-to-energy conversion efficiency, η. The focus of the Slone & Netzer (2012) work is the effect of disc winds on the emitted SEDs. Here we do not consider disc winds because of the lack of far UV spectroscopy required to deduce their presence and because we focus on slim disc where there are additional large uncertainties (see below). As in Slone & Netzer (2012), our calculations include Comptonization of the emitted radiation at every point in the disc atmosphere and,for BH spin values of $a_\star > 0$, full General Relativistic corrections. For retrograde discs with $a_\star < 0$, the general relativity effects are not included, which is a fair approximation given the large size of the ISCO ($> 6r_g$, where $r_g = GM_{BH}/c^2$ is the gravitational radius of the black hole). Apart from Comptonization, the calculations do not include any other radiative transfer in the disc atmosphere that can make significant changes to the far UV SED (e.g. Davis & Laor 2011, Fig. 2).

Standard, Shakura & Sunyaev (1973) thin accretion disc models are limited to $\dot{m} \leq 0.3$. Beyond this accretion rate, the disc geometry becomes thick and many of the approximation used in the model no-longer hold (see Laor & Netzer 1989, and references therein). As explained in Section 1, the main differences between thin and slim discs are the thicker geometry, due to the much larger radiation pressure in the disc, and the way the radiation escapes the system. This includes radial advection and perhaps saturation of the emitted luminosity. Unfortunately, detailed SED calculations of

slim discs are highly simplified and hardly available. A recent detailed model of this type is discussed in Wang et al. (2014a). According to this and earlier models, the long wavelength part of the SED originates outside of the thick part of the disc and is, therefore, very similar in its shape to the thin AD SED. For small BH mass systems, significant differences between the two appear only at very short wavelengths, beyond the Lyman limit. The special geometry dictates strong anisotropy in such systems, much beyond the standard AD anisotropy due to inclination. This, again, is most noticeable at short wavelengths (see Fig. 4 in Wang et al. 2014b). The observations discussed here do not include the wavelength range below λ=1000Å and hence we use the thin AD model for the fitting of the SED over this range. Later on, when we discuss the Lyman continuum emission, we consider the various possibilities regarding slim discs.

As explained earlier, theoretical slim disc models are still highly simplistic and are not in very good agreement with state-of-the-art numerical calculations like those of Sądowski & Narayan (2015). Given this fundamental uncertainty, we treat all derived quantities that depend on the short wavelength part of the model, e.g. the bolometric luminosity and Eddington ratio, as the most uncertain parameters for the sub-sample of 16 SEAMBHs described in this work.

4.2 Fitting procedure

We used the Slone & Netzer (2012) code described earlier to calculate a large number of thin disc spectra that include the entire range of BH mass, accretion rate and spin expected in our sample. The input for the fit include, for each source, the black hole mass (M_{BH} in units of $M_{\odot}$), and the mass accretion rate ($\dot{M}$ in units of $M_{\odot}$/yr). We used the RM-based masses and the measured (from the 5100Å continuum) accretion rates listed in Du et al. (2015, see Table 7). The uncertainty on the mass is estimated to be a factor of $\sim$3 due to the the uncertainties on the measured time lags, the measured FWHM(Hβ), and the uncertainties in the conversion of observed broad line profiles to a "mean gas velocity" (the f_{BLR} term in $M_{BH} = f_{BLR}\, c\tau\, FWHM(H\beta)^2/G$). The accretion rate is obtained from the luminosity at rest-wavelength 5100Å using the method described in Davis & Laor (2011) as detailed in Netzer & Trakhtenbrot (2014, see Eqn. 1 there). We assumed a factor three uncertainty on the accretion rate derived in this way which is a combination of flux uncertainty (mostly stellar light subtraction), the unknown inclination, and the fact that the chosen wavelength (5100Å) is not on the $L_{\nu} \propto \nu^{1/3}$ part of the SED.

All sources fitted in this work are type-I AGN which are assumed to be observed close to face-on. The range of inclination is roughly 0–60 degree and the range in $\cos(\theta)$ 0.5–1. We assumed the anisotropy function proposed by Netzer & Trakhtenbrot (2014),

$$f(\theta) = \frac{f_0 F_{\nu}}{F_{\nu}(\text{face-on})} = f_0\, \frac{\cos\theta\,(1+b(\nu)\cos\theta)}{1+b(\nu)} \qquad (2)$$

with $b(\nu) = 2$, $f_0 = 1.2 \times 10^{30}$ erg/s/Hz, and $\cos\theta = 0.75$ for all sources. The remaining parameters are the BH spin and intrinsic reddening. We experimented with the full range of spin parameters, from -1 to 0.998. Because of the fitted range of wavelengths, which is far from the frequency of maximum disc temperature, there is very little difference between different spin value. We therefore show, for each source only two values, $a_{\star} = -1$ and $a_{\star} = 0.998$.

The fitting procedure includes the comparison of the observed SED with various combinations of disc SEDs covering the range of mass, accretion rate, and the two chosen spins and assumed reddening. The reddening is taken into account by changing $E(B-V)$ in steps of 0.004 mag, calculating, for each value, a new mass accretion rate and its range of uncertainty. A simple χ^2 procedure was used to find the best-fit combination of reddening and thin AD models. We use at least three line-free windows covering the optical spectroscopic data, and all the available photometric data. The line-free windows are centred on 4205Å, 5100Å and 6855Å, with widths ranging from 10 to 30Å. For those objects with no photometric data, three additional line-free continuum windows were used: 5620Å, 6205Å and 6860Å. For the error on each continuum point, we combine the standard error from the Poison noise, an assumed 5% error on the flux calibration, and the relative error of 20% on the combination of the uncertainties on the host-galaxy contribution and the unknown stellar population. To allow for the large elapsed time between the GALEX and the optical observations, which increases the uncertainty due to source variability, we added an uncertainty of 20% to the GALEX fluxes. Note that this is not meant to take into account the real variations between epoch since this is dealt with, in our special method described in Section 3.1 where we provide more information about the way we used the best SED that avoids, as much as possible, the variability issue. We refer the reader to Appendix B for a detailed description of the fitting results for individual sources.

5 RESULTS

The samples described here were selected from the RM AGN sample with high accretion rate, $\dot{\mathcal{M}} \geq 3$ (super-Eddington) and with sub-Eddington accretion rate $\dot{\mathcal{M}} < 3$. In the following we use the normalized Eddington ratio, $\dot{m} = \eta\dot{\mathcal{M}}$, which allow an easy comparison with previous works. While not all data are of the same quality, we were able to secure photometric and spectroscopic data that cover the 0.2-20 μm range for all sources. For 8 sources (4 sub-Eddington and 4 super-Eddington) we have both simultaneous and non-simultaneous optical/UV photometry. In the following discussions we do not distinguish between simultaneous and non-simultaneous SEDs.

Our best fitted disc SEDs are shown in Figure A1 and all the model parameters, including the virialized M_{BH} and $\dot{M}$, are listed in Table A1. Two models are listed per source, corresponding to the minimum and maximum spin parameter. The error bars on the intrinsic reddening enclose the 68% confidence range. Finally, the average spectral properties for both groups and for the entire sample are summarized in Table 2. In the following plots, for every derived thin AD model parameter we display the mean between the higher and lower values corresponding to the minimum and maximum spin, and the uncertainly which represents the range of possible values.

Table 2. Median Parameters for super-Eddington (13), sub-Eddington (16) AGN and the entire sample (29). The uncertainties reflect the 16^{th} and 84^{th} percentiles. When saturation (Eqn. 1) is taken into account the parameter is tagged with the term $_{sat}$. Two numbers are listed for each thin AD model corresponding to the minimum and the maximum spin. The unabsorbed luminosity at 2 keV is given by the best-fit power law over the hard X-ray band (2-10 keV).

PARAMETER	super-Eddington		sub-Eddington		all	
	$a_\star = 0.998$	$a_\star = -1$	$a_\star = 0.998$	$a_\star = -1$	$a_\star = 0.998$	$a_\star = -1$
reverberation-mapped resutls						
$\log \lambda L_\lambda(5100\text{Å})$	$44.00^{+0.23}_{-0.69}$	$44.00^{+0.23}_{-0.69}$	$43.68^{+0.32}_{-0.51}$	$43.68^{+0.32}_{-0.51}$	$43.71^{+0.50}_{-0.55}$	$43.71^{+0.50}_{-0.55}$
z	$0.054^{+0.078}_{-0.022}$	$0.054^{+0.078}_{-0.022}$	$0.031^{+0.017}_{-0.009}$	$0.031^{+0.017}_{-0.009}$	$0.035^{+0.081}_{-0.009}$	$0.035^{+0.081}_{-0.009}$
$\log M_{BH}$	$6.86^{+0.35}_{-0.38}$	$6.86^{+0.35}_{-0.38}$	$7.97^{+0.13}_{-0.71}$	$7.97^{+0.13}_{-0.71}$	$7.16^{+0.85}_{-0.51}$	$7.16^{+0.85}_{-0.51}$
$\log \dot{\mathcal{M}}$	$1.61^{+0.98}_{-0.77}$	$1.60^{+0.98}_{-0.77}$	$-0.70^{+0.35}_{-0.38}$	$-0.72^{+0.37}_{-0.36}$	$0.84^{+1.24}_{-1.68}$	$0.83^{+1.23}_{-1.69}$
power-law modelling						
β_{UV}	$2.13^{+0.37}_{-0.36}$	$2.13^{+0.37}_{-0.36}$	$2.12^{+0.36}_{-0.30}$	$2.12^{+0.36}_{-0.30}$	$2.12^{+0.39}_{-0.34}$	$2.12^{+0.39}_{-0.34}$
$E(B-V)$ /PL/	$0.00^{+0.06}_{-0.00}$	$0.00^{+0.06}_{-0.00}$	$0.00^{+0.00}_{-0.00}$	$0.00^{+0.00}_{-0.00}$	$0.00^{+0.00}_{-0.00}$	$0.00^{+0.00}_{-0.00}$
thin AD modelling						
$E(B-V)$	$0.07^{+0.06}_{-0.03}$	$0.06^{+0.06}_{-0.02}$	$0.01^{+0.03}_{-0.01}$	$0.00^{+0.00}_{-0.00}$	$0.05^{+0.04}_{-0.05}$	$0.04^{+0.06}_{-0.04}$
$\log M_{BH}$	$7.25^{+0.28}_{-0.46}$	$7.26^{+0.26}_{-0.46}$	$7.88^{+0.13}_{-0.60}$	$7.80^{+0.44}_{-0.52}$	$7.32^{+0.65}_{-0.52}$	$7.36^{+0.59}_{-0.56}$
$\log \dot{\mathcal{M}}$	$1.81^{+0.46}_{-1.43}$	$1.80^{+0.58}_{-1.22}$	$-0.62^{+0.98}_{-0.44}$	$-0.32^{+0.66}_{-0.58}$	$0.36^{+1.72}_{-1.07}$	$0.50^{+1.62}_{-1.03}$
$\log L_{\text{Lyman}}$	$46.55^{+0.46}_{-0.92}$	$45.57^{+0.62}_{-0.96}$	$44.96^{+0.45}_{-0.50}$	$43.70^{+0.32}_{-0.96}$	$45.59^{+1.29}_{-0.81}$	$44.48^{+1.40}_{-1.11}$
$\log L_{\text{Lyman,sat}}$	$45.84^{+0.19}_{-0.39}$	$45.78^{+0.29}_{-1.17}$	$44.96^{+0.45}_{-0.50}$	$43.70^{+0.32}_{-0.96}$	$45.52^{+0.37}_{-0.74}$	$44.48^{+1.43}_{-1.11}$
$\langle h\nu \rangle$	$11.8^{+2.7}_{-7.0}$	$3.2^{+1.0}_{-1.5}$	$2.4^{+2.7}_{-0.3}$	$1.3^{+0.5}_{-0.1}$	$5.3^{+8.5}_{-3.0}$	$1.8^{+2.3}_{-0.5}$
$\kappa_{5100\text{Å}}$	208^{+475}_{-171}	61^{+71}_{-53}	17^{+45}_{-5}	3^{+7}_{-1}	62^{+373}_{-46}	10^{+90}_{-7}
$\kappa_{5100\text{Å},sat}$	53^{+51}_{-32}	65^{+61}_{-57}	18^{+46}_{-5}	3^{+7}_{-1}	32^{+51}_{-19}	10^{+95}_{-7}
$\log \lambda L_\lambda(5100\text{Å})$ (erg/s)	$44.23^{+0.37}_{-0.52}$	$43.93^{+0.44}_{-0.47}$	$43.64^{+0.63}_{-0.33}$	$43.63^{+0.64}_{-0.41}$	$43.90^{+0.59}_{-0.51}$	$43.83^{+0.51}_{-0.55}$
$\log \lambda L_\lambda(2500\text{Å})$ (erg/s)	$44.51^{+0.24}_{-0.25}$	$44.48^{+0.28}_{-0.25}$	$43.95^{+0.24}_{-0.25}$	$43.89^{+0.29}_{-0.27}$	$44.15^{+0.46}_{-0.43}$	$44.12^{+0.44}_{-0.49}$
L_{AGN} (erg/s)	$46.56^{+0.46}_{-0.90}$	$45.65^{+0.57}_{-0.79}$	$45.07^{+0.49}_{-0.44}$	$44.28^{+0.35}_{-0.44}$	$45.65^{+1.23}_{-0.78}$	$44.84^{+1.10}_{-0.72}$
$L_{AGN,sat}$ (erg/s)	$45.89^{+0.19}_{-0.42}$	$45.82^{+0.29}_{-0.95}$	$45.07^{+0.49}_{-0.44}$	$44.28^{+0.35}_{-0.44}$	$45.56^{+0.38}_{-0.69}$	$44.84^{+1.11}_{-0.72}$
$\Delta \log M_{BH}$ †	$0.31^{+0.19}_{-0.24}$	$0.31^{+0.19}_{-0.22}$	$-0.11^{+0.37}_{-0.19}$	$-0.04^{+0.29}_{-0.14}$	$0.15^{+0.34}_{-0.36}$	$0.19^{+0.28}_{-0.31}$
$\Delta \log \dot{\mathcal{M}}$ ‡	$-0.24^{+0.58}_{-0.33}$	$-0.13^{+0.47}_{-0.32}$	$0.59^{+0.23}_{-1.06}$	$0.54^{+0.15}_{-0.62}$	$-0.01^{+0.68}_{-0.55}$	$0.13^{+0.49}_{-0.46}$
Luminosities						
L_{trous} (erg/s)	$44.52^{+0.50}_{-0.36}$	$44.52^{+0.50}_{-0.36}$	$44.53^{+0.37}_{-0.47}$	$44.53^{+0.37}_{-0.47}$	$44.53^{+0.48}_{-0.44}$	$44.53^{+0.48}_{-0.44}$
$\log L_\nu(5\mu m)$ (erg/s)	$43.99^{+0.50}_{-0.38}$	$43.99^{+0.50}_{-0.38}$	$43.86^{+0.52}_{-0.39}$	$43.86^{+0.52}_{-0.39}$	$43.86^{+0.62}_{-0.35}$	$43.86^{+0.62}_{-0.35}$
$\log L_\nu(2keV)$ (erg/s)	$43.23^{+0.10}_{-0.40}$	$43.23^{+0.10}_{-0.40}$	$42.85^{+0.57}_{-0.40}$	$42.85^{+0.57}_{-0.40}$	$43.19^{+0.22}_{-0.64}$	$43.19^{+0.22}_{-0.64}$

† Defined as $\Delta \log M_{BH} \equiv (\log M_{BH})^{\text{fit}} - (\log M_{BH})^{\text{virial}}$

‡ Defined as $\Delta \log \dot{\mathcal{M}} \equiv (\log \dot{\mathcal{M}})^{\text{fit}} - (\log \dot{\mathcal{M}})^{\text{virial}}$

5.1 Accretion Disc SED

A major goal of this project is to determine what fraction of sub-Eddington and super-Eddington accretors in our sample can be fit by the simple optically thick, geometrically thin AD model based on their long wavelength SEDs. By allowing intrinsic reddening as a free parameter of the thin AD model, we can fit all the 29 sources of our sample. For 23 sources, our modelling requires some reddening and for 6 sources, which are all sub-Eddington AGN, the amount of reddening is consistent with zero. We found that 14% of the RM-selected AGN are consistent with $E(B-V)> 0.1$ in good agreement with the work of Krawczyk et al. (2015) where the SED was modelled by a single power law. Indeed, the reddening distribution of our entire sample is also consistent with that presented by Lusso et al. (2013, Figure 3). Several of the declared good fits still include small deviations of the model from the local continuum at some wavelengths. This is not surprising given the uncertainties on AD models, especially the radiative transfer in the disc atmosphere that was not treated here, as well as on the choice of the host galaxy template. In general, the simple χ^2-fitting procedure cannot distinguish between $a_\star = -1$ and $a_\star = 0.998$, given the assumed uncertainties on BH mass, BH accretion rate, reddening and the long wavelengths used for the fitting. Observations at shorter wavelengths (i.e. extreme-UV $\lambda < 2000$Å) are clearly required to make such a distinction.

For consistency with previous works, the 0.2-1 μm SED was also fitted using a single reddened power-law model ($L_\nu \propto \nu^{-\alpha_{UV}}$). A satisfactory fit ($\chi^2_\nu < 2$) with $A_V = 0$ is found for 86% (25/29) of the sources. The remaining four objects (which are super-Eddington) were successfully fit-

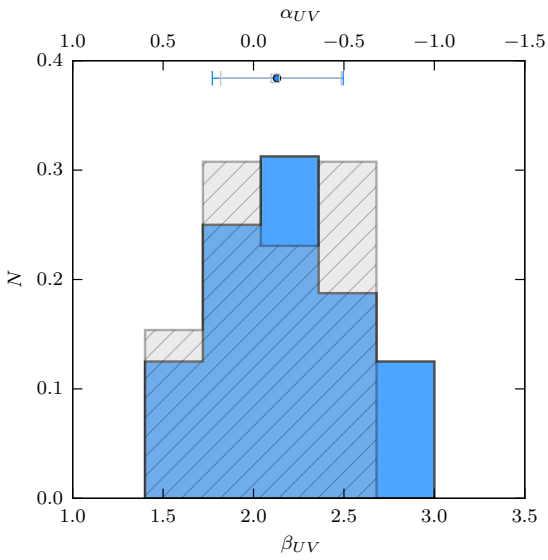

Figure 2. The distribution of optical to UV spectral indices in the super-Eddington and sub-Eddington objects. The spectral indices are defined such that $L_\lambda \propto \lambda^{-\beta_{UV}}$ and $\beta_{UV} = 2 - \alpha_{UV}$. Colour code as Figure 1.

ted with $A_V > 0$. The reddening distribution of the entire sample is quite consistent, as in the case of the thin AD modelling, with that presented in various earlier studies, e.g. Lusso et al. (2013). The range of slopes is large, from $\alpha_{UV} = 0.55$ to $\alpha_{UV} = -0.98$. The Kolmogorov-Smirnov test shows that the optical to UV spectral index corrected for intrinsic reddening for SEAMBHs and sub-Eddington accretors are fully consistent (see Figure 2), with means $\langle\alpha_{UV}\rangle = -0.14$ and -0.10 and a standard deviations of $\sigma = 0.40$ and 0.33, respectively. A comparison with earlier works on much larger samples (Vanden Berk et al. 2001; Grupe et al. 2010) shows that our sample has bluer optical/UV continua.

5.2 Properties of the obscuring dust

If the adopted thin AD model does indeed explain the emitted SED of AGN in our sample, then dust in the host galaxies of approximately 50% of the AGN in our sample is contributing to the reddening of the optical-UV spectrum. It is therefore interesting to test the nature of the dust which is causing the extinction. Several earlier studies (Hopkins et al. 2004; Glikman et al. 2012) claimed that an SMC-type extinction curve best accounts for the reddening, in preference to MW-type or Gaskell et al. (2004) reddening, Capellupo et al. (2015) find that in their sample of 39 z=1.5 AGN, there were no cases where the SMC-type curve allowed for a better fit than either the MW or simple power-law extinction curve. Our observations indicate that for those AGN that require intrinsic reddening, there is no preference for one particular extinction curve. This is probably because the UV observations are based on photometry instead of spectroscopy and may also be the result of the limited wavelength range which is essential to differentiate between the various extinction laws.

As noted above, the amount of extinction seems to be more significant in super-Eddington AGN. Figure 3 compares the reddening distribution of the super-Eddington and the sub-Eddington groups assuming a SMC extinction curve. The median reddening for the super-Eddington sources is $\langle E(B-V)\rangle = 0.07$ mag with a scatter of $\sigma = 0.08$, while the sub-Eddington AGN sample shows $\langle E(B-V)\rangle \approx 0.01$ mag with $\sigma = 0.01$. A Kolmogorov-Smirnov test rules out the hypothesis that both groups are drawn from the same distribution of $E(B-V)$ with a probability of $> 99.9\%$. Experimenting with other extinction curves give basically the same distribution shown in Figure 3.

5.3 Uncertainties in black hole mass

In order to evaluate the goodness of our fit, we have analysed the black hole properties recovered by the thin AD fit. We find that the measured "virialized" mass black hole and mass accretion rate, within the allowed uncertainties, lead to a suitable disc model for all the 29 AGN. The comparisons are shown in Figure 4. The median deviation of the black hole mass ($\Delta \log M_{BH} \equiv \log M_{BH,\rm fit} - \log M_{BH,\rm virial}$) for the super-Eddington sources is 0.305 dex with a 16^{th} and 84^{th} percentile of 0.07 and 0.5 dex, while the median for the sub-Eddington sources is -0.07 dex with its percentiles at -0.23 and 0.25 dex. There is no systematic shift on the mass accretion rate which is uniformly distributed. This is because the accretion rate in the disc model is directly related to the observed luminosity and the best mass estimate. Note also that the assumed inclination of $\cos(\theta) = 0.75$ only introduce an additional uncertainty on the fitting results and can not explain the shift on the black hole mass observed in the super-Eddington group.
Finally, it is interesting to note that our thin AD fit recover almost perfectly both the black hole mass and the mass accretion rate. This is in contrast with what has been found in the work of Calderone et al. (2013), which claims that the best-fit black hole mass is on average a factor of ∼6 greater than the corresponding virialized mass estimation.

5.4 Ionizing Continuum

An additional consistency check of the fitted SEDs can be obtained by studying the disc ionizing continuum which is directly related to the observed emission lines. The relative intensity of the lines, as well as their equivalent widths are related to the mean energy of the ionizing photons, the ionization parameter and the covering factor by gas near the BH. The hydrogen Lyman continuum as the part of the SED responsible for most of the heating and ionization of the broad emission-line gas can be derived from our disc SEDs. In particular, we can calculate both Lyman continuum, L_{Lyman}, and the mean energy of an ionizing photon, $\langle h\nu\rangle$, and compare the distribution of these numbers in the two groups.

A comparison of the Lyman continuum properties of the two groups is shown in Figure 5 where both parameters are plotted against the normalized Eddington ratio. For comparison, the mean energy of an ionizing photon with an optical/UV power-law SED of slope $\alpha_\nu = 1.5$ is 2.31 Ryd. As expected, the super-Eddington group, with its higher accretion rate and smaller BH mass, are predicted to have

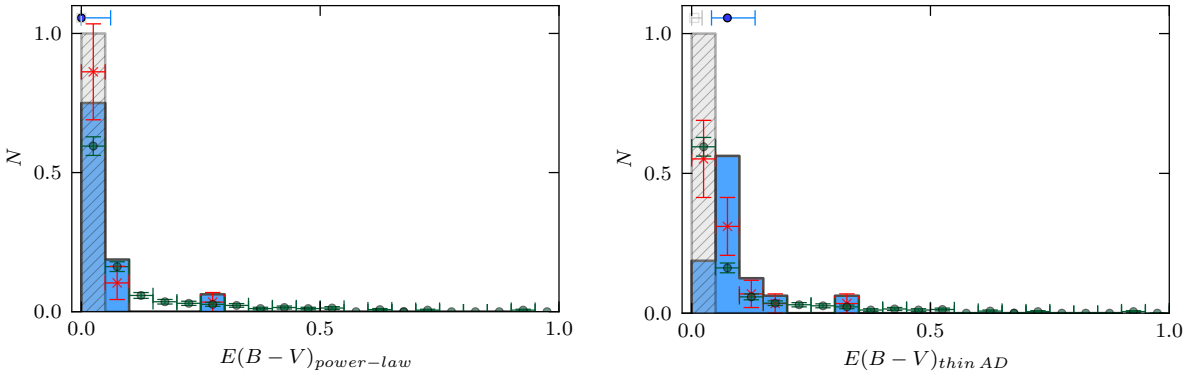

Figure 3. Intrinsic reddening E(B-V) distribution modelled by a classical SMC-like extinction curve with $R_V = 2.74$. The amount of reddening was derived from model fittings assuming a single power law (*left*) and a thin AD model (*right*). The red crosses with error bars represent the reddening distribution for the entire sample (29 objects) and the green circles with error bars show the distribution of $E(B-V)$ presented by Lusso et al. (2013). Histogram colour code as in Fig. 1.

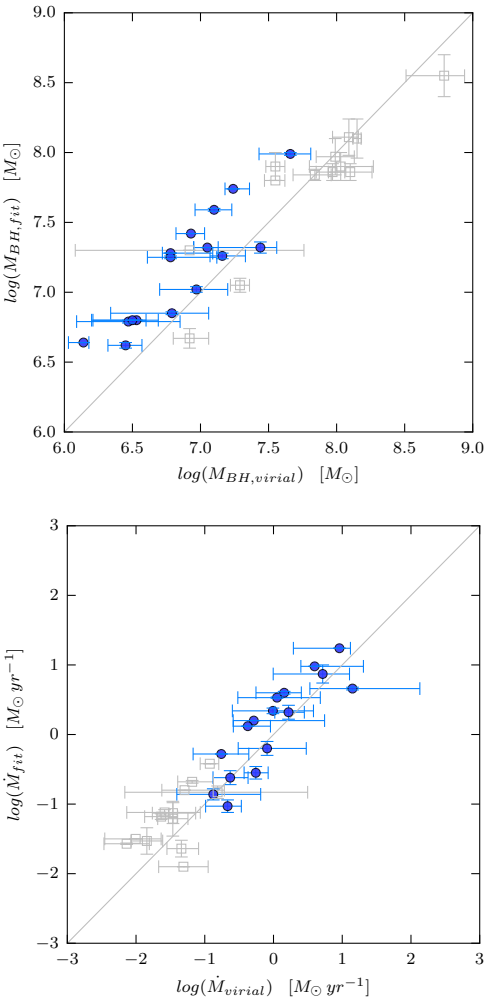

Figure 4. Comparison of the virialized black hole mass (*top*) and the dimensionless mass accretion rate (*bottom*) against those given by our best-fit thin AD model. The straight lines indicate the 1:1 ratios. Gray-blue circles represent super-Eddington AGN and gray-empty squares sub-Eddington AGN.

larger $L_{\rm Lyman}/L_{\rm AGN}$ and higher $\langle h\nu \rangle$. The diagrams show a very strong trends with the mass accretion rate. This is in line with the results of V09, although their sample is in the lower-Eddington ratio regime. The average ionization fraction is ∼0.5 for the lowest Eddington ratio $\dot{\mathcal{M}} \leq 3$ (similar with V09) and rise to ∼0.9 for the highest $\dot{\mathcal{M}} > 3$.

Here, and in all other results related to the Lyman continuum, the soft X-ray emission, and the bolometric correction factors and torus covering factors discussed below, we must take into account two important factors related to the highly simplified assumption of the high energy part of the SED in super-Eddington sources. First, the entire disc structure can change at high accretion rate, leading to two-component disc like the one proposed by Done et al. (2012). This possibility is not investigated here, partly because of the large uncertainties on such models and mostly because of the lack of short wavelength observations. Second, saturation, if exists, affects the far-UV SED much more than the near-UV and optical continuum (Du et al. 2015, and references therein). In this scenario the bolometric luminosity for sources with $\dot{\mathcal{M}} > 20$ has only a weak logarithmic dependency on the mass accretion rate (Eqn. 1). Such values of $\dot{\mathcal{M}}$ are found in most of the super-Eddington sources in our sample (11/16, see Table A1). The case of saturation is compared with the thin AD predictions in Figure 5, and comparison with the other relevant quantities are shown in Figs. 6 and 7. Indeed it results in lower Lyman continuum bolometric correction factors and torus covering factors (see below). However, all these are still considerably higher than the values estimated for the sub-Eddington sources. Note that we do not have a simple way of estimating the changes in the mean energy of the ionizing photons in cases of saturation and hence do no comment of this additional effects.

In principle, the higher expected $L_{\rm Lyman}/L_{\rm AGN}$ and $\langle h\nu \rangle$ for super-Eddington sources could be investigated by comparing line intensities and EWs between the two groups. One prediction is that, given similar BLR covering factors, super-Eddington sources will show larger line EWs and stronger lines of highly ionized species. While this general issue is beyond the scope of the present work, we note that such differences in EWs have never been reported. In fact, several studies show tends in the opposite directions (see

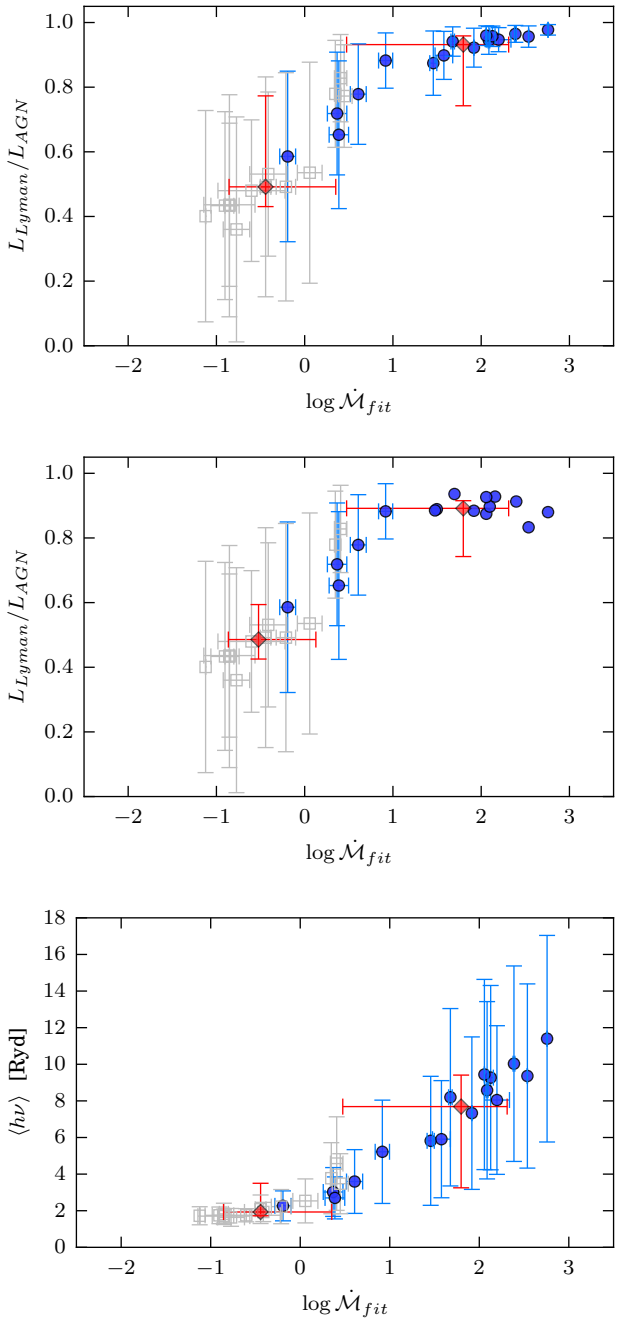

Figure 5. Lyman continuum luminosity fraction for cases of no saturation (*top*) and saturation according to Eqn. 1 (*midle*). The mean energy of an ionizing photon as a function of the normalized Eddington ratio for the cases of the no saturation is shown at the bottom. The red diamond represents the median parameter for each group and the error bars correspond to the 16^{th} and 84^{th} percentile. Gray-blue circles represent super-Eddington AGN and grey-empty squares sub-Eddington AGN.

e.g. Du et al. 2014).

5.5 Bolometric Correction factors

Our disc models can also be used to determine the bolometric correction factors for the objects in question. Such factors are used in many AGN studies (Marconi et al. 2004; Netzer & Trakhtenbrot 2014) as a way to deduce the bolometric luminosity, $L_{\rm AGN}$, in those cases (basically all cases) where much of the SED is not directly observed. Bolometric corrections are frequently given as

$$\kappa_\nu = \frac{L_{\rm AGN}}{\nu L_\nu} \tag{3}$$

where $L_{\rm AGN}$ is the intrinsic bolometric luminosity obtained from the best-fit thin AD model. Here we report κ_ν relative to 5100Å, 3000Å and 1400Å (see Table A1). Unfortunately, our limited wavelength coverage does not allow us to distinguish between the spins which is the main uncertainty on the bolometric correction factors. The difference in efficiency between the two extreme spin values amount to about a factor 8.4.

Figure 6 shows the distribution of the bolometric correction factor as a function of mass accretion rate. In general, κ_{5100} has a very wide distribution where, for the sub-Eddington group, the values are distributed around the "standard" value of about 10 used in many earlier studies like Kaspi et al. (2000); Marconi et al. (2004); Trakhtenbrot & Netzer (2012). There is a clear tendency for a larger κ_{5100} in the group of super-Eddington sources due to the significantly higher accretion rate for a given BH mass. This results in a shift of the SED to shorter wavelength and a considerable increase in κ_{5100}. For this group, a more typical value is about 150. As explained, there are large uncertainties in calculated disc SEDs for such sources since their large $L_{\rm AGN}/L_{Edd}$ suggests they contain slim rather than thin ADs. In particular, we must consider the possibility of saturation for $\dot{\mathcal{M}} > 20$. In this case the bolometric correction factor at 5100Å is considerably smaller, about 60 instead of 150 (see bottom panel of Fig. 6).

5.6 Torus emission and SED

We also tested the possible differences between sub-Eddington and super-Eddington sources by investigating their torus emission. This is done by using the most recent available WISE All-Sky Data Release that covers >99% of the sky. The torus SED was constructed from the four WISE bands, at 3.6, 4.5, 12 and 22 μm, using only data with a signal-to-noise ratio SNR>20. The observed IR SED were modelled by the torus template of Mor & Netzer (2012) which is made of three components: a clumpy torus, a dusty narrow line region, and a hot pure-graphite dust component which represent the innermost part of the torus. In general, this SED is similar to other torus SEDs, e.g. those used by Mullaney et al. (2011) and Lira et al. (2013) except that none of these models include the hot graphite dust and hence cannot provide a proper fit to the short wavelength part at around 1-3 μm. Given the lack of adequate spectral resolution, there is no way to take into account the contribution of star-formation emission in the host galaxy. In addition, we do not have good enough spatial information to isolate the nuclear AGN emission from star formation in the host galaxies. These points were discussed in detail in Sani et al. (2011)

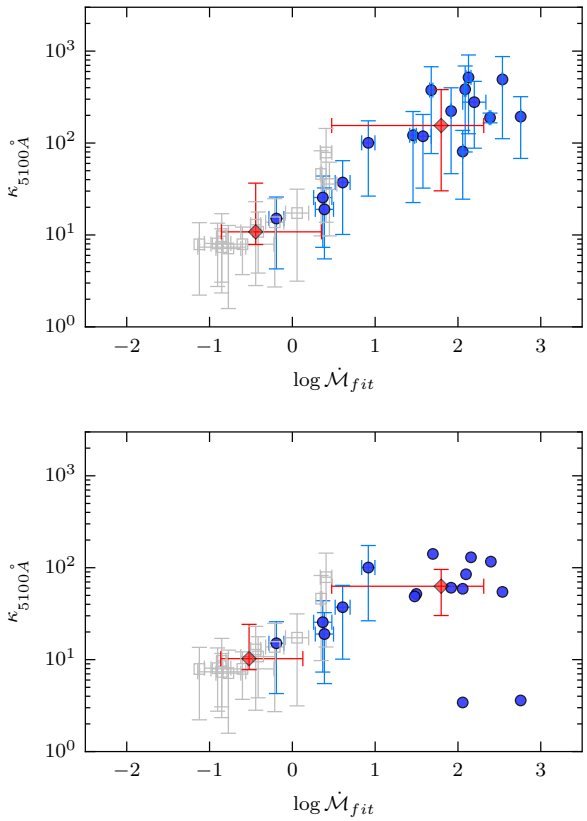

Figure 6. Bolometric correction at 5100Å as a function of the Eddington ratio for the best-fit thin AD models on the top panel and the case of saturation at the bottom. Colour code as in Fig. 5.

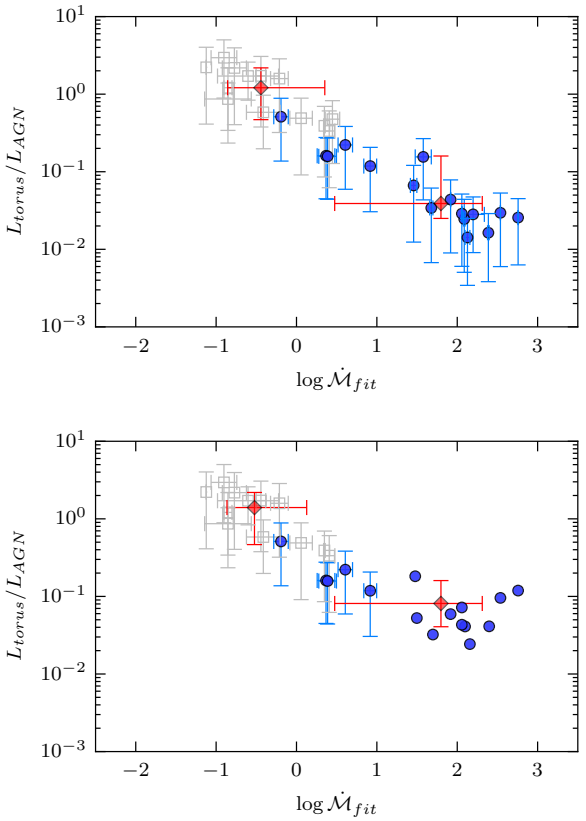

Figure 7. The torus luminosity fraction, defined as $L_{torus}/L_{\rm AGN}$ and assuming complete isotropy for the dust emission, as a function of the normalized Eddington ratio (top no saturation, bottom saturation according to Eqn. 1). Colour code as in Fig. 5.

and Mor & Netzer (2012) where a much larger number of low and high Eddington ratio (NLS1s) AGN are considered.

The fitting procedure is based on the use of three templates, the mean torus SED and its 25^{th} and 75^{th} percentiles. In this procedure, the normalization is the only additional free parameter and its value is determined by a χ^2 analysis. This procedure has been recently discussed in great detail by Nezer et al. (2015). Earlier attempts are described in Mullaney et al. (2011); Lusso et al. (2013); Roseboom et al. (2013); Tsai et al. (2015) and others.

We find that in all 29 cases, one of the three templates gave a satisfactory fit to the observed near- and mid-IR. Figure 8 shows the median torus AGN for both groups which was constructed from the best-fit templates. In general, the observed SEDs are very similar but the mid-IR spectrum of SEAMBHs is somewhat bluer.

Given the torus SED we can compare the torus covering factor of super-Eddington and sub-Eddington sources. In general, this depends on the emission pattern of the torus and hence on deviations from isotropy (Netzer 2015, and references therein). For the purpose of the present paper we assume complete isotropy and compare the integrated 1-200 μm emission of the torus, $L_{\rm torus}$, with $\lambda L_\lambda(5100\text{Å})$ and $L_{\rm AGN}$ of each source. For the torus model used here $L_{torus}/L_{5\mu m} = 3.58$ for the median composite, 3.18 for the bluer composite and 4.27 for the redder composite. The comparison of $L_{torus}/\lambda L_\lambda(5100\text{Å})$ in the two groups suggest very similar distribution (see Table 2). On the other hand $L_{\rm torus}/L_{\rm AGN}$, which is related to the torus covering factor, show lower fractions for super-Eddington AGN (see Figure 7) because of their larger κ_{5100}. As discussed below, this difference suggest either saturation (Eqn. 1) or that the far-UV luminosity of the super-Eddington is over-estimated by a large factor.

5.7 Simultaneous Optical/UV and X-ray Observations

The AGN paradigm includes a thermal accretion disc emitting in the optical-UV and a corona which up-scatters the emitted disc photons to X-ray energies resulting in a power-law X-ray emission. Studies of large AGN samples show a clear dependence of α_{OX} (the spectral index connecting the 2500Å and 2 keV emission) on the UV luminosity such that higher $L_\nu(2500)$ corresponds to weaker 2 keV emission (see Steffen et al. 2006; Grupe et al. 2010, and references therein). In this paper we treat the 2-10 keV emission in a simplistic way and focus on α_{OX}. In a forthcoming publication we provide more information about the X-ray spectral shape including new XMM-Newton observations for some of the sources.

We calculate the optical-to-X-ray spectral slope α_{OX} for 17 sources that have simultaneous X-ray spectrum and OM photometry and show them in Figure 9 against the rest-frame luminosity at 2500Å, the normalized Edding-

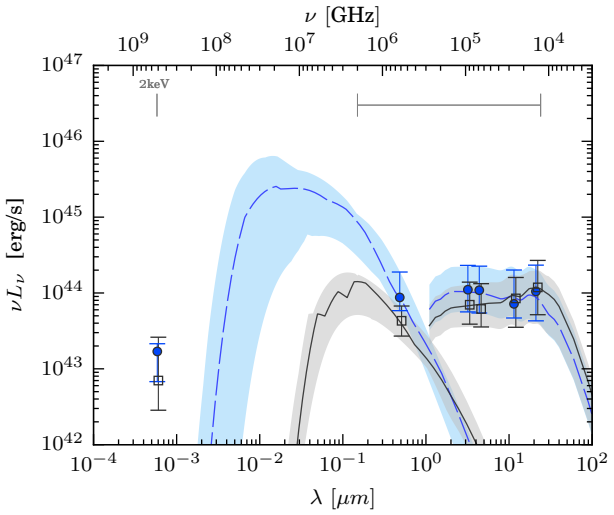

Figure 8. Median AGN SEDs for the two groups: blue, dashed line represents super-Eddington and black, solid line sub-Eddington. The shaded areas show the 25^{th} and 75^{th} percentiles. The circle (super-Eddington) and square (sub-Eddington) points represent the median luminosity at 2 keV, 5100Å, 3.6 μm, 4.5 μm, 12 μm and 22 μm. The X-ray luminosity at 2 keV was computed assuming a single power-law between 2-10 keV corrected for galactic absorption. The horizontal line displays the spectral window used to fit both thin AD model and the torus templates. The displayed median disc SED is assuming the minimum spin ($a_\star = -1$).

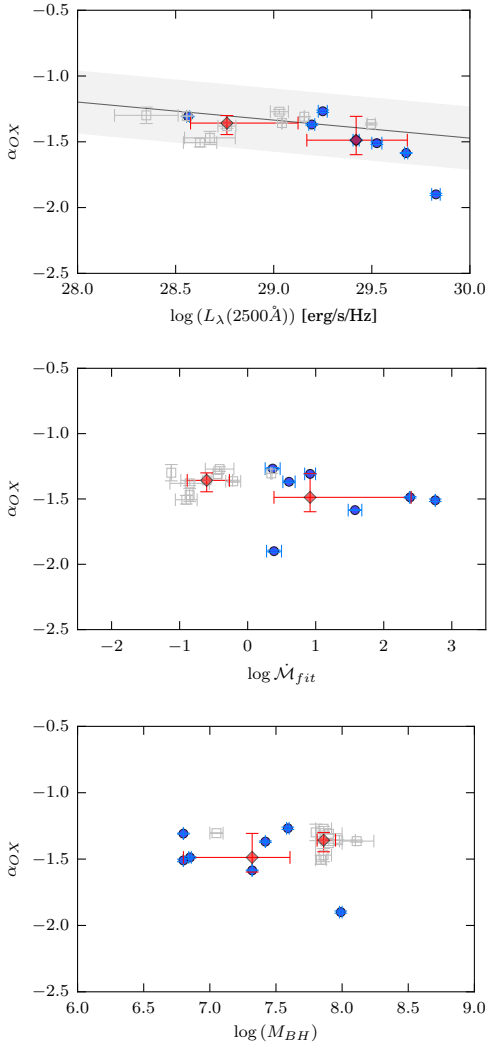

Figure 9. α_{OX} as a function of the rest-frame luminosity at 2500Å (*top*), the normalized Eddington ratio (*middle*) and the black hole mass (*bottom*). The solid line and shaded area in the top panel show the best fit and spread obtained by Steffen et al. (2006) for a sample of optically selected AGN. Colour code as in Fig. 1. The two outliers with the smallest α_{OX} are NGC 7469 and PG 0844.

ton ratio and the black hole mass. The X-ray luminosities were derived from the absorption-corrected rest-frame 2-10 keV fluxes which was modelled with a single power law accounting for Galactic absorption. Except for two sources (NGC 7469, and PG 0844+349), the values of α_{OX} corrected for intrinsic reddening lie within the scatter expected from Steffen et al. (2006) which reinforce the importance of accounting for dust extinction (V09, Grupe et al. 2010). There are reasons to suspect the reliability of α_{OX} for the two outliers. The X-ray spectrum of NGC 7469 shows sign of high absorption which could explain their lower optical-to-X-ray spectral slope. For PG 0844 there is an inconsistency between the optical spectrum and the OM photometry that suggest a large uncertainty due to SED variations. We point the reader to Appendix B for a more detailed explanation. Interestingly, the distribution of α_{OX} shows no large differences between sub-Eddington and super-Eddington sources with an average α_{OX} of -1.36 and -1.48, respectively. In contrast with V09, we do not find any correlation between α_{OX} and the black hole mass.

6 DISCUSSION AND CONCLUSIONS

We have presented SEDs for a sample of AGN selected for their accretion rate from a variety of reverberation mapping campaigns. We define a group of super-Eddington AGN thought to be powered by slim accretion discs because of their extremely high Eddington ratio, and compared them to sub-Eddington AGN thought to be powered by thin accretion discs. The unique aspect of the work is the detailed comparison with high accretion rate AGN with BH mass measured from direct RM. We have 16 objects of this group which triples the number of such objects known in previous studies. The 5 keV to 10000Å spectral energy distribution modelled here is, in our opinion, the best way to compare thin and slim disc models and to test the various suggestions for the extreme properties of slim discs at the far-UV. A very detailed study of the intrinsic SED of very high accretion rate AGN, like those studied here, has never been done before. We are able to improve the SED modelling by employing the most accurate measurements of mass accretion rate and black hole mass, as well as simultaneous optical-to-UV photometry in conjunction with high resolution optical spectra. These are useful for determining the degree of host-galaxy contamination and for constrain better the intrinsic reddening of the sources.

In general we find that the host galaxy contribution spans a fairly wide range of values, but the optical/UV emission lines are unlikely to contaminate the underlying disc continuum. The simultaneous and non-simultaneous optical-to-UV (0.2-1 μm) data, allowed us to fit thin AD models, including both Galactic and intrinsic extinction, to all 29 RM-selected AGN: 13 sub-Eddington sources and 16 super-Eddington sources.

We find that in the lower-Eddington ratio regime ($\dot{m} < 0.3$) the estimated intrinsic dust extinction is consistent with zero in approximately 46% of the sources. The fractional number, and the median $E(B-V)$ are similar to those obtained in earlier and larger samples of AGN that used different types of SEDs. For the high accretion rate AGN ($\dot{m} \geq 0.3$) we find that at least 75% (12/16) of these require significant optical-UV dust reddening. On average, the level of dust extinction in the super-Eddington group is higher than that of the slow accreting AGN.

As in earlier studies that combine accretion disc and corona models, we confirm that those AGN with higher accretion rate and smaller BH mass present larger reddening-corrected ionizing fractions, $L_{\rm Lyman}/L_{\rm AGN}$. The actual number depends on the importance of saturation in the super-Eddington sources. Another related conclusion is that super-Eddington sources show higher mean energy of the ionizing photons and larger bolometric correction factors. In this fast accreting AGN sample, the 5100Å bolometric corrections is an order of magnitude larger than the factors found for sub-Eddington sources, depending on the importance of saturation. This correlation factor is considerably larger than the "standard" value used in many earlier studies based on low Eddington ratio sample. Note that our approach does not take into account the contribution of the X-ray emission and extrapolate the thin AD models to far-UV energies. A useful extension of this work would be to acquire simultaneous HST observations at shorter wavelengths, potentially improving the extreme-UV SED shape and reveal clues about the nature of slim accretion disc.

Our study shows that for 15/17 objects with simultaneous UV-X-ray observations, there is no correlation between α_{OX} with accretion rate or black hole mass. Part of this may be related to the reddening correction used in this work mostly for large $\dot{m}$ AGN. In particular, our study does not confirm the correlation of α_{OX} with black hole mass suggested in V09.

We find no statistical evidence that the torus SED in super-Eddington AGN is different from the one in sub-Eddington AGN, although the median torus SED is marginally bluer (see Figure 8). Moreover, the medians $L_{5\mu m}/L_{5100\text{Å}}$ of the two groups are very similar. However, there is a very significant difference in the derived tours covering factors, with super-Eddington sources showing much smaller $L_{\rm torus}/L_{\rm AGN}$ by as much as an order of magnitude even when considering saturation. This is basically the same result obtained for the $L_{5100\text{Å}}$ bolometric correction factor and is directly related to the predicted, but so far unobserved far-UV emission of super-Eddington objects.

There are two major conclusions to the present study. First, thin AD models can be used to obtain satisfactory fits to the 0.2-1 μm SEDs of all AGN, whether sub-Eddington or super-Eddington accretors. This is generally consistent with the few available, albeit not very accurate calculated slim accretion disc 0.2-1 μm SEDs that show them to be generally similar to SEDs of thin ADs (Wang et al. 2014b, and references therein). Second, several of the important results obtained here, that are related to the high energy (Lyman continuum) part of the SED, including $L_{\rm Lyman}/L_{\rm AGN}$, the mean energy of the ionizing photons, and the bolometric correction factors, all suggest large differences between the two groups. However, these are not direct observations but rather inferences from model assumptions about the part of the continuum, below about 0.2-1 μm, which is not accessible to us. It is quite likely that the total emitted high frequency radiation in super-Eddington AGN is smaller than assumed here, and its angular dependence may be different too.

We find two indications that the above differences between the groups found here may be related to wrong or uncertain model assumptions. The emission line intensities, or line EWs of super-Eddington sources are not significantly different from those of sub-Eddington sources. This point was not addressed in detail in the present work, but is well known in earlier studies of large samples of NLS1, like Grupe et al. (2010). In fact, various studies (e.g. Du et al. 2015) show that the EW(Hβ) in super-Eddington sources is somewhat smaller than in sub-Eddington AGN. Strong angular dependence of the SED in a system with a flat BLR whose covering factor is small is one possible explanation. The second is the finding that $L_{\rm torus}/L_{\rm AGN}$ (or, equivalently the torus covering factor) is smaller in super-Eddington sources. However, $L_{\rm torus}/\lambda L_{\lambda}(5100\text{Å})$ of the two groups is very similar. We find it hard to believe that the increase in $L_{\rm AGN}$ is exactly compensated for by a decrease in the (geometrical) covering factor of the torus. A more likely explanation is that the emitted $L_{\rm Lyman}$ radiation in SEAMBHs is either much weaker than assumed here, due to saturation, or strongly angle dependent -two possibilities that have been raised in earlier studies (e.g. Wang et al. 2014b). While we prefer the latter explanation, the very good agreement of $L_{\rm torus}/\lambda L_{\lambda}(5100\text{Å})$ between the two groups suggest fine tuning that is hard to accept.

ACKNOWLEDGEMENTS

We thank the anonymous referee for providing a positive and useful report which has clarified our discussion and improved this paper.Funding for this work has been provided by a joint ISF-NSFC grant number 83/13. We are grateful to Du Pu for help with the Lijiang data and to Brad Peterson for help with the AGN Watch data.

REFERENCES

Abramowicz M. A., Czerny B., Lasota J. P., Szuszkiewicz E., 1988, ApJ, 332, 646
Bentz M. C., Peterson B. M., Netzer H., Pogge R. W., Vestergaard M., 2009, ApJ, 697, 160
Bentz M. C., et al., 2013, ApJ, 767, 149
Blaes O., Hubeny I., Agol E., Krolik J. H., 2001, ApJ, 563, 560
Brocksopp C., Starling R. L. C., Schady P., Mason K. O., Romero-Colmenero E., Puchnarewicz E. M., 2006, MNRAS, 366, 953
Calderone G., Ghisellini G., Colpi M., Dotti M., 2013, MNRAS, 431, 210

Capellupo D. M., Netzer H., Lira P., Trakhtenbrot B., Mejía-Restrepo J., 2015, MNRAS, 446, 3427
Cardelli J. A., Clayton G. C., Mathis J. S., 1989, ApJ, 345, 245
Charlot S., Bruzual A. G., 1991, ApJ, 367, 126
Collinson J. S., Ward M. J., Done C., Landt H., Elvis M., McDowell J. C., 2015, MNRAS, 449, 2174
Davis S. W., Laor A., 2011, ApJ, 728, 98
Davis S. W., Woo J.-H., Blaes O. M., 2007, ApJ, 668, 682
Dietrich M., Hamann F., Shields J. C., Constantin A., Vestergaard M., Chaffee F., Foltz C. B., Junkkarinen V. T., 2002, ApJ, 581, 912
Done C., Davis S. W., Jin C., Blaes O., Ward M., 2012, MNRAS, 420, 1848
Du P., et al., 2014, ApJ, 782, 45
Du P., et al., 2015, ApJ, 806, 22
Elvis M., et al., 1994, ApJS, 95, 1
Elvis M., et al., 2012, ApJ, 759, 6
Fanali R., Caccianiga A., Severgnini P., Della Ceca R., Marchese E., Carrera F. J., Corral A., Mateos S., 2013, MNRAS, 433, 648
Gallo L. C., 2006, MNRAS, 368, 479
Gaskell C. M., Goosmann R. W., Antonucci R. R. J., Whysong D. H., 2004, ApJ, 616, 147
Glikman E., et al., 2012, ApJ, 757, 51
Gordon K. D., Clayton G. C., Misselt K. A., Landolt A. U., Wolff M. J., 2003, ApJ, 594, 279
Grupe D., Wills B. J., Wills D., Beuermann K., 1998, A&A, 333, 827
Grupe D., Komossa S., Leighly K. M., Page K. L., 2010, ApJS, 187, 64
Hopkins P. F., et al., 2004, AJ, 128, 1112
Jin C., Ward M., Done C., 2012, MNRAS, 425, 907
Jin C., Done C., Ward M., 2016, MNRAS, 455, 691
Kaspi S., Smith P. S., Netzer H., Maoz D., Jannuzi B. T., Giveon U., 2000, ApJ, 533, 631
Koratkar A., Blaes O., 1999, PASP, 111, 1
Krawczyk C. M., Richards G. T., Gallagher S. C., Leighly K. M., Hewett P. C., Ross N. P., Hall P. B., 2015, AJ, 149, 203
Laor A., Davis S. W., 2011, MNRAS, 417, 681
Laor A., Netzer H., 1989, MNRAS, 238, 897
Lira P., Videla L., Wu Y., Alonso-Herrero A., Alexander D. M., Ward M., 2013, ApJ, 764, 159
Lusso E., et al., 2013, ApJ, 777, 86
Marchese E., Della Ceca R., Caccianiga A., Severgnini P., Corral A., Fanali R., 2012, A&A, 539, A48
Marconi A., Risaliti G., Gilli R., Hunt L. K., Maiolino R., Salvati M., 2004, MNRAS, 351, 169
Mineshige S., Kawaguchi T., Takeuchi M., Hayashida K., 2000, PASJ, 52, 499
Mor R., Netzer H., 2012, MNRAS, 420, 526
Mullaney J. R., Alexander D. M., Goulding A. D., Hickox R. C., 2011, MNRAS, 414, 1082
Netzer H., 2015, ARA&A, 53, 365
Netzer H., Trakhtenbrot B., 2014, MNRAS, 438, 672
Peterson B. M., Wanders I., Bertram R., Hunley J. F., Pogge R. W., Wagner R. M., 1998, ApJ, 501, 82
Peterson B. M., et al., 1999, ApJ, 510, 659
Pogge R. W., 2000, New Astron. Rev., 44, 381
Richards G. T., et al., 2006, ApJS, 166, 470
Roseboom I. G., Lawrence A., Elvis M., Petty S., Shen Y., Hao H., 2013, MNRAS, 429, 1494
Sani E., Lutz D., Risaliti G., Netzer H., Gallo L. C., Trakhtenbrot B., Sturm E., Boller T., 2010, MNRAS, 403, 1246
Sani E., Marconi A., Hunt L. K., Risaliti G., 2011, MNRAS, 413, 1479
Santos-Lleó M., et al., 1997, ApJS, 112, 271
Sądowski A., Narayan R., 2015, MNRAS, 454, 2372
Sądowski A., Narayan R., McKinney J. C., Tchekhovskoy A., 2014, MNRAS, 439, 503
Shakura N. I., Sunyaev R. A., 1973, A&A, 24, 337
Shang Z., et al., 2005, ApJ, 619, 41
Shen Y., et al., 2011, ApJS, 194, 45
Slone O., Netzer H., 2012, MNRAS, 426, 656
Steffen A. T., Strateva I., Brandt W. N., Alexander D. M., Koekemoer A. M., Lehmer B. D., Schneider D. P., Vignali C., 2006, AJ, 131, 2826
Sulentic J. W., Zwitter T., Marziani P., Dultzin-Hacyan D., 2000, ApJ, 536, L5
Thorne K. S., 1974, ApJ, 191, 507
Trakhtenbrot B., Netzer H., 2012, MNRAS, 427, 3081
Tsai C.-W., et al., 2015, ApJ, 805, 90
Vanden Berk D. E., et al., 2001, AJ, 122, 549
Vasudevan R. V., Fabian A. C., 2007, MNRAS, 381, 1235
Vasudevan R. V., Fabian A. C., 2009, MNRAS, 392, 1124
Vasudevan R. V., Mushotzky R. F., Winter L. M., Fabian A. C., 2009, MNRAS, 399, 1553 (V09)
Wang J.-M., et al., 2014a, ApJ, 793, 108
Wang J.-M., Qiu J., Du P., Ho L. C., 2014b, ApJ, 797, 65
Zheng W., Kriss G. A., Telfer R. C., Grimes J. P., Davidsen A. F., 1997, ApJ, 475, 469

APPENDIX A: THIN AD RESULTS

In this Appendix, we present the results of our fitting thin AD models to all sources. Two numbers are listed per source and parameter, corresponding to minimum ($a_\star = -1.0$) and maximum ($a_\star = 0.998$) spin parameters. The difference in efficiency between the two amount to about a factor 8.4. For each source, the best-fit SED is also shown in Figure A1.

Table A1. super-Eddington group: Measured and deduced physical parameters modelling the intrinsic reddening $E(B-V)$ with a classical SMC extinction curve and assuming an inclination of $\cos\theta$=0.75. Two thin AD models are listed for each sources corresponding to maximum ($a_\star = 0.998$) and minimum ($a_\star$=-1) spin; the later correspond to the second row.

	RM results		Host Galaxy		Power-Law model			thin AD model													
Object	$\log M_{BH}$	$\log \dot{\mathcal{M}}$	template	f†	E(B-V)	β_{UV}‡	χ^2_ν	E(B-V)	$\log M_{BH}$	$\log \dot{\mathcal{M}}$	χ^2_ν	$\log L_{\rm AGN}$	$L_{\rm Lyman}/L_{\rm AGN}$	$\kappa_{5100\text{Å}}$	$\kappa_{3000\text{Å}}$	$\kappa_{1400\text{Å}}$	$\langle h\nu\rangle$	$\log L_{5100\text{Å}}$	$\log L_{2500\text{Å}}$	$\log L_{2keV}$	$\log L_{5\mu m}$
	$[M_\odot]$								$[M_\odot]$			[erg/s]					Ryd	erg/s	erg/s	erg/s	erg/s
Mrk142	$6.47^{+0.38}_{-0.38}$	$2.10^{+0.59}_{-0.59}$	ssp_11Gyr_z05	0.30	0.00	2.07 ± 0.19	0.998	$0.09^{+0.02}_{-0.02}$	6.78	2.10	0.174	46.60	0.99	907.54	259.02	63.26	14.30	43.64	44.31		43.61
								$0.09^{+0.01}_{-0.02}$	6.80	2.16	0.167	45.74	0.93	126.18	36.88	9.42	4.24	43.64	44.30		43.61
Mrk335	$6.93^{+0.10}_{-0.11}$	$1.39^{+0.18}_{-0.17}$	ssp_11Gyr_z05	0.24	0.00	1.58 ± 0.34	0.050	$0.07^{+0.07}_{-0.03}$	7.42	0.52	0.054	45.71	0.93	64.26	30.54	12.30	5.34	43.90	44.29	43.31	43.96
								$0.06^{+0.07}_{-0.03}$	7.42	0.70	0.056	44.90	0.62	10.12	4.94	2.20	1.85	43.89	44.26	43.31	43.96
Mrk382	$6.50^{+0.19}_{-0.29}$	$1.20^{+0.69}_{-0.53}$	ssp_11Gyr_z02	0.52	0.00	2.43 ± 0.20	0.979	$0.01^{+0.04}_{-0.01}$	6.80	0.84	0.794	45.41	0.97	174.46	66.43	23.83	8.04	43.17	43.65	42.84	43.22
								$0.01^{+0.04}_{-0.01}$	6.80	1.00	0.795	44.58	0.80	26.47	10.19	3.78	2.40	43.16	43.63	42.84	43.22
Mrk486	$7.24^{+0.12}_{-0.06}$	$0.67^{+0.20}_{-0.32}$	ssp_11Gyr_z05	0.31	0.00	1.84 ± 0.42	0.246	$0.07^{+0.16}_{-0.05}$	7.74	−0.28	0.245	45.23	0.85	25.86	13.55	5.62	3.08	43.82	44.16		43.84
								$0.04^{+0.16}_{-0.04}$	7.74	−0.10	0.251	44.42	0.32	4.28	2.44	1.36	1.45	43.79	47.07		43.84
Mrk493	$6.14^{+0.04}_{-0.11}$	$2.06^{+0.33}_{-0.21}$	ssp_11Gyr_z05	0.38	0.00	1.96 ± 0.12	1.946	$0.10^{+0.01}_{-0.01}$	6.64	2.06	0.191	46.41	0.99	24.49	287.00	67.10	14.64	45.02	44.09		43.61
								$0.08^{+0.01}_{-0.01}$	6.64	2.06	0.871	45.48	0.93	137.15	39.58	9.81	4.25	43.34	44.01		43.61
Mrk1044	$6.45^{+0.12}_{-0.13}$	$1.37^{+0.40}_{-0.41}$	ssp_11Gyr_z05	0.43	0.00	2.14 ± 0.22	0.982	$0.08^{+0.02}_{-0.06}$	6.60	1.70	0.109	46.04	0.99	676.15	200.50	52.41	13.04	43.21	43.86		43.34
								$0.07^{+0.02}_{-0.05}$	6.64	1.66	0.118	45.08	0.90	76.80	24.01	6.87	3.35	43.19	43.81		43.34
IRAS04416	$6.78^{+0.31}_{-0.06}$	$2.76^{+0.16}_{-0.67}$	ssp_11Gyr_z02	0.38	0.05	2.98 ± 0.09	1.946	$0.07^{+0.01}_{-0.02}$	7.28	2.54	1.331	47.55	0.99	872.42	254.02	66.27	14.39	44.61	45.27		44.74
								$0.05^{+0.01}_{-0.01}$	7.28	2.54	1.721	46.60	0.92	111.48	33.44	9.16	4.33	44.55	45.20		44.74
IRASF12397	$6.79^{+0.27}_{-0.45}$	$2.94^{+0.98}_{-0.62}$	ssp_11Gyr_z05	0.52	0.27	2.54 ± 0.35	1.020	$0.35^{+0.05}_{-0.03}$	6.84	2.38	0.139	46.92	0.99	211.56	333.89	75.88	15.37	44.59	44.51	43.23	43.82
								$0.35^{+0.06}_{-0.03}$	6.86	2.40	0.135	46.04	0.94	165.90	46.98	11.29	4.69	43.82	44.48	43.23	43.82
J075101	$7.16^{+0.17}_{-0.09}$	$1.57^{+0.25}_{-0.41}$	ssp_11Gyr_z02	0.35	0.08	2.39 ± 0.19	1.990	$0.12^{+0.01}_{-0.04}$	7.24	1.92	0.118	46.92	0.98	399.02	130.52	41.19	11.50	44.32	44.87		44.29
								$0.12^{+0.01}_{-0.03}$	7.28	1.92	0.134	45.98	0.86	46.42	15.98	5.36	3.17	44.31	44.51		44.29
J080101	$6.78^{+0.34}_{-0.17}$	$2.51^{+0.39}_{-0.72}$	ssp_11Gyr_z05	0.27	0.00	2.74 ± 0.43	0.131	$0.10^{+0.08}_{-0.09}$	7.26	2.06	0.152	47.08	0.98	468.74	149.35	45.45	12.11	44.40	45.01		44.51
								$0.11^{+0.06}_{-0.09}$	7.24	2.34	0.152	46.36	0.91	87.91	27.22	7.86	3.99	44.41	45.04		44.51
J081441	$6.97^{+0.23}_{-0.27}$	$1.66^{+0.63}_{-0.57}$	ssp_11Gyr_z02	0.56	0.00	2.28 ± 0.24	1.331	$0.05^{+0.02}_{-0.05}$	7.00	2.10	0.159	46.84	0.99	688.69	205.30	55.06	13.42	44.00	44.65		44.02
								$0.05^{+0.02}_{-0.05}$	7.04	2.08	0.171	45.90	0.90	79.94	24.99	7.25	3.74	44.00	44.62		44.02
J081456	$7.44^{+0.12}_{-0.49}$	$0.85^{+1.03}_{-0.30}$	ssp_11Gyr_z02	0.49	0.07	1.74 ± 0.26	1.977	$0.14^{+0.02}_{-0.03}$	7.28	1.50	0.196	46.55	0.97	220.18	80.63	28.91	9.34	44.20	44.73		44.06
								$0.13^{+0.01}_{-0.03}$	7.36	1.42	0.248	45.56	0.77	22.51	9.01	3.45	2.29	44.21	44.68		44.06
J093922	$6.53^{+0.07}_{-0.33}$	$2.65^{+0.71}_{-0.20}$	ssp_11Gyr_z02	0.50	0.00	2.12 ± 0.20	0.414	$0.06^{+0.01}_{-0.01}$	6.80	2.76	1.843	47.19	0.99	67.99	537.70	106.64	17.04	45.36	44.63	43.28	44.47
								$0.05^{+0.01}_{-0.00}$	6.80	2.76	2.259	46.34	0.96	319.34	84.76	17.58	5.75	43.83	44.58	43.28	44.47
PG0844	$7.66^{+0.15}_{-0.23}$	$0.82^{+0.57}_{-0.42}$	ssp_11Gyr_z02	0.22	0.00	1.45 ± 0.36	0.494	$0.17^{+0.15}_{-0.08}$	8.00	0.28	0.362	46.05	0.88	32.48	16.90	7.09	3.85	44.54	44.93	42.56	44.17
								$0.16^{+0.14}_{-0.07}$	7.98	0.50	0.365	45.26	0.42	5.49	3.01	1.54	1.55	44.52	44.88	42.56	44.17
PG2130	$7.05^{+0.08}_{-0.10}$	$1.75^{+0.23}_{-0.20}$	ssp_11Gyr_z02	0.54	0.00	2.22 ± 0.26	0.715	$0.03^{+0.04}_{-0.03}$	7.32	1.48	0.237	46.57	0.97	204.56	76.13	27.75	9.11	44.26	44.75	43.23	44.62
								$0.04^{+0.03}_{-0.04}$	7.32	1.68	0.237	45.78	0.82	32.33	11.96	4.31	2.71	44.27	44.76	43.23	44.62
Mrk110	$7.10^{+0.13}_{-0.14}$	$0.85^{+0.26}_{-0.25}$	ssp_11Gyr_z05	0.50	0.00	1.82 ± 0.25	0.048	$0.04^{+0.05}_{-0.03}$	7.60	0.26	0.039	45.63	0.91	43.75	22.07	9.03	4.36	43.99	44.35	43.63	43.76
								$0.03^{+0.04}_{-0.03}$	7.58	0.48	0.038	44.84	0.53	7.33	3.83	1.81	1.69	43.97	44.31	43.63	43.76

† Host galaxy contribution to the observed flux at 5100Å.

‡ Optical to UV spectral slope defined such that $L_\lambda \propto \lambda^{-\beta_{UV}}$, $\beta_{UV} = 2 - \alpha_{UV}$ and $L_\nu \propto \nu^{-\alpha_{UV}}$.

Table A1. sub-Eddington group: Measured and deduced physical parameters modelling the intrinsic reddening $E(B-V)$ with a classical SMC extinction curve and assuming an inclination of $\cos\theta$=0.75. Two thin AD models are listed for each sources corresponding to maximum ($a_\star = 0.998$) and minimum ($a_\star$=-1) spin; the later correspond to the second row.

	RM results		Host Galaxy		Power-Law model			thin AD model													
Object	$\log M_{BH}$	$\log \dot{\mathcal{M}}$	template	f†	E(B-V)	β_{UV}‡	χ^2_ν	E(B-V)	$\log M_{BH}$	$\log \dot{\mathcal{M}}$	χ^2_ν	$\log L_{\rm AGN}$	$L_{\rm Lyman}/L_{\rm AGN}$	$\kappa_{5100\text{Å}}$	$\kappa_{3000\text{Å}}$	$\kappa_{1400\text{Å}}$	$\langle h\nu\rangle$	$\log L_{5100\text{Å}}$	$\log L_{2500\text{Å}}$	$\log L_{2keV}$	$\log L_{5\mu m}$
	$[M_\odot]$								$[M_\odot]$			[erg/s]					Ryd	erg/s	erg/s	erg/s	erg/s
Mrk79	$7.84\pm^{0.12}_{0.16}$	$-0.60\pm^{0.25}_{0.21}$	ssp_11Gyr_z05	0.24	0.00	1.56 ± 0.28	0.507	$0.04\pm^{0.03}_{0.02}$	7.88	−1.06	0.549	44.59	0.72	13.42	7.20	3.15	2.20	43.46	43.79	42.39	43.86
								$0.00\pm^{0.03}_{0.00}$	7.80	−0.74	0.612	43.84	0.14	2.75	1.70	1.26	1.29	43.40	43.62	42.39	43.86
Mrk279	$7.97\pm^{0.09}_{0.12}$	$-0.86\pm^{0.33}_{0.30}$	ssp_11Gyr_z02	0.33	0.00	1.84 ± 0.37	0.324	$0.02\pm^{0.03}_{0.02}$	7.92	−0.62	0.268	45.07	0.79	17.77	9.43	3.99	2.46	43.82	44.15	43.40	43.69
								$0.00\pm^{0.01}_{0.00}$	7.80	−0.20	0.303	44.38	0.28	3.85	2.23	1.31	1.41	43.79	44.06	43.40	43.69
Mrk290	$7.55\pm^{0.07}_{0.07}$	$-0.82\pm^{0.23}_{0.23}$	ssp_11Gyr_z02	0.28	0.00	1.94 ± 0.20	0.189	$0.02\pm^{0.02}_{0.02}$	8.00	−1.14	0.079	44.63	0.69	11.68	6.31	2.81	2.08	43.56	43.89	42.85	43.58
								$0.00\pm^{0.01}_{0.00}$	7.80	−0.56	0.146	44.02	0.18	3.07	1.85	1.26	1.33	43.53	43.79	42.85	43.58
Mrk509	$8.15\pm^{0.03}_{0.03}$	$-0.50\pm^{0.13}_{0.14}$	ssp_11Gyr_z02	0.35	0.00	2.12 ± 0.26	0.350	$0.01\pm^{0.02}_{0.01}$	7.96	0.20	0.200	45.93	0.88	31.49	16.39	6.86	3.74	44.43	44.77		44.36
								$0.00\pm^{0.01}_{0.00}$	8.24	−0.08	0.383	44.94	0.19	3.14	1.89	1.26	1.33	44.44	44.69		44.36
Mrk590	$7.55\pm^{0.07}_{0.08}$	$-0.28\pm^{0.36}_{0.36}$	ssp_11Gyr_z05	0.62	0.00	2.02 ± 4.65	1.452	$0.07\pm^{0.01}_{0.01}$	7.80	−1.12	4.553	44.45	0.73	13.61	7.30	3.19	2.22	43.32	43.59	42.65	43.39
								$0.00\pm^{0.00}_{0.00}$	7.80	−1.12	2.445	43.46	0.07	2.22	1.46	1.37	1.23	43.11	43.27	42.65	43.39
Mrk817	$7.99\pm^{0.14}_{0.14}$	$-0.88\pm^{0.22}_{0.22}$	ssp_11Gyr_z05	0.41	0.00	2.16 ± 0.22	0.757	$0.00\pm^{0.02}_{0.00}$	8.10	−0.98	0.452	44.89	0.70	12.17	6.55	2.90	2.11	43.80	44.12	43.19	44.14
								$0.00\pm^{0.00}_{0.00}$	7.84	−0.22	2.192	44.40	0.26	3.70	2.16	1.30	1.39	43.83	44.12	43.19	44.14
Mrk1511	$7.29\pm^{0.07}_{0.07}$	$-0.35\pm^{0.24}_{0.24}$	ssp_11Gyr_z05	0.44	0.00	2.48 ± 0.19	1.832	$0.00\pm^{0.01}_{0.00}$	7.00	0.36	1.544	45.13	0.94	82.35	37.08	14.51	5.72	43.21	43.64	42.84	43.48
								$0.00\pm^{0.00}_{0.00}$	7.10	0.34	1.855	44.22	0.61	9.77	4.80	2.15	1.83	43.23	43.64	42.84	43.48
NGC5548	$8.10\pm^{0.16}_{0.16}$	$-1.66\pm^{0.33}_{0.33}$	ssp_11Gyr_z05	0.34	0.00	1.57 ± 0.47	0.057	$0.08\pm^{0.04}_{0.02}$	7.80	−0.80	0.030	44.77	0.78	17.03	9.05	3.84	2.41	43.54	43.88	42.53	43.55
								$0.01\pm^{0.07}_{0.01}$	7.92	−0.90	0.014	43.80	0.09	2.34	1.52	1.32	1.25	43.43	43.62	42.53	43.55
NGC7469	$6.92\pm^{0.84}_{0.84}$	$0.84\pm^{1.31}_{1.35}$	ssp_11Gyr_z02	0.70	0.00	1.90 ± 0.28	0.167	$0.05\pm^{0.11}_{0.04}$	7.30	0.36	0.025	45.43	0.93	61.84	29.54	11.84	5.11	43.64	44.02	40.64	43.86
								$0.04\pm^{0.10}_{0.04}$	7.30	0.54	0.024	44.62	0.61	9.77	4.80	2.15	1.83	43.63	43.99	40.64	43.86
PG1229	$8.03\pm^{0.24}_{0.23}$	$-1.04\pm^{0.52}_{0.55}$	ssp_11Gyr_z02	0.40	0.00	2.60 ± 0.16	0.710	$0.00\pm^{0.00}_{0.00}$	7.80	−0.38	1.815	45.19	0.83	23.01	12.11	5.05	2.86	43.83	44.23	43.43	44.09
								$0.00\pm^{0.00}_{0.00}$	8.00	−0.50	5.231	44.28	0.15	2.82	1.73	1.26	1.30	43.83	44.23	43.43	44.09
PG1617	$8.79\pm^{0.15}_{0.28}$	$-1.51\pm^{0.58}_{0.33}$	ssp_11Gyr_z02	0.33	0.00	2.41 ± 0.17	1.236	$0.00\pm^{0.00}_{0.00}$	8.40	−0.62	1.588	45.55	0.71	12.68	6.81	2.98	2.12	44.45	44.77		44.63
								$0.00\pm^{0.00}_{0.00}$	8.70	−0.92	17.081	44.56	0.01	1.58	1.26	2.28	1.15	44.36	44.42		44.63
Fairall9	$8.09\pm^{0.07}_{0.12}$	$-0.70\pm^{0.31}_{0.21}$	ssp_11Gyr_z02	0.32	0.00	2.14 ± 0.43	0.020	$0.01\pm^{0.05}_{0.01}$	7.98	−0.10	0.006	45.65	0.84	24.79	13.03	5.46	3.16	44.25	44.60	43.63	44.57
								$0.00\pm^{0.02}_{0.00}$	8.24	−0.32	0.161	44.70	0.14	2.72	1.69	1.26	1.29	44.26	44.56	43.63	44.57
MCG+06	$6.92\pm^{0.14}_{0.12}$	$-0.35\pm^{0.37}_{0.45}$	ssp_11Gyr_z05	0.51	0.00	2.54 ± 0.24	1.676	$0.00\pm^{0.01}_{0.00}$	6.60	0.48	0.899	44.85	0.96	144.10	57.10	20.89	7.13	42.69	43.13		43.12
								$0.00\pm^{0.01}_{0.00}$	6.74	0.34	1.306	43.86	0.69	13.74	6.23	2.63	2.02	42.72	43.13		43.12

† Host galaxy contribution to the observed flux at 5100Å.

‡ Optical to UV spectral slope defined such that $L_\lambda \propto \lambda^{-\beta_{UV}}$, $\beta_{UV} = 2 - \alpha_{UV}$ and $L_\nu \propto \nu^{-\alpha_{UV}}$.

APPENDIX B: NOTES ON INDIVIDUAL OBJECTS

Additional information regarding available data. Table B1 show the best-fit thin AD model for those sources with more than one possible dataset.

Mrk 335

Mrk 335 was observed three times by the OM aboard of the *XMM-Newton* which allow us to fit three independent and simultaneous datasets and compare it with the non-simultaneous SED form by the mean optical spectrum and the GALEX photometry. The simultaneous datasets show variability at a level of 20% over a 9 year period. The best-fit thin AD model results achieved with the non-simultaneous SED are firmly consistent with the shapes of the simultaneous SED and both contemporaneous and non-contemporaneous SED shapes claim for a considerable amount of intrinsic extinction in order to ensure satisfactory fit ($A_V = 0.37 - 0.15$). The contemporaneous SED datasets show larger A_V values.

IRAS F12397+3333

IRAS F12397+3333 is an IR luminous source and as such shows *redder* optical SED compared with most AGN, including those in the sample. Both simultaneous and non-simultaneous SED fit results show that a satisfactory fit will not be reached unless a significant dust attenuation is assumed. The hypothesis of notable intrinsic reddening is supported by polarization measurements, as well as by a steep Balmer Decrement (Grupe et al. 1998; Du et al. 2015).

J093922

The good agreement between the near-UV GALEX flux with the OM photometric point (temporally separated by ∼1 year) allow us to use both in conjunction with the optical spectrum and assume that it is the most convenient approach to model the optical/UV underlying continuum.

PG 2130

The good agreement between the near-UV GALEX flux with the two OM photometric points (UVW2, UVM2) and the low statistics of the simultaneous dataset lead us to believe that a non-simultaneous dataset is the best procedure to study the optical/UV emission. The simultaneous SED shape, which consist of only four photometric points, is consistent to that found by fitting this non-contemporaneous dataset.

PG 0844

PG 0844 is the only source where the optical/UV broadband SED could not be modelled by thin AD spectrum. The inconsistent on the time-lag measurements from line-to-line (see Peterson et al. 1999) as well as the residuals on the Balmer narrow-emission lines in this object turns the reverberation mapping results to be of rather low quality. Thus, the Hβ BLR size measurement is considered unreliable and does not enable us to find a satisfactory fit to the optical/UV OM photometric points. We believe that the unreliable time-lag measurements enable to find an accurate black hole mass measurements.

Mrk 110

The optical spectrum was taken in the lowest flux state, whilst both GALEX and XMM-Newton observed Mrk 110 in higher flux states. The optical observations show variability of a factor ∼10 over a 3 year period. Therefore the simultaneous SED composed by six OM photometric points is the only possible dataset. Although the GALEX photometry was not fitted they are in good agreement with the contemporaneous optical/UV SED shape.

Mrk 79

The optical spectrum was taken in the lowest flux state, whilst both GALEX and XMM-Newton observed Mrk 79 in a higher flux states. The narrower spectral window of Mrk 79 and the large observed variability between the mean optical spectrum and the photometry rules out the spectrum. Taking advantage of the good agreement between the near-UV GALEX flux and the OM photometry, a non-simultaneous dataset is probably the best SED to study the accretion disc emission. Indeed, the low number of simultaneous photometric points does not allow to construct a contemporaneous dataset.

Mrk 279

The OM photometric flux at the effective wavelength 3444Å seems to be in a lower flux state when it is compared with the optical spectrum. This 20% of variability between both spectrum and OM photometry prevent to join both datasets. Two non-simultaneous SED were constructed: on the one hand, GALEX in conjunction with the simultaneous OM photometric band; on the other, a fit over the single optical spectrum adding another two line-free points. The fitting results of both datasets are in good agreement and no intrinsic reddening was necessary to get a satisfactory thin AD fit.

Mrk 509

There is a variability of a factor ∼2 between simultaneous OM observations over a 9 year period. From the OM observations, we can see how both optical spectrum and GALEX photometry seem to follow the lowest flux state rather than a higher one. In addition to the contemporaneous data set given by the OM observation in the 2009, we also fitted a non-simultaneous dataset which consists of the GALEX photometric data in conjunction with the optical spectrum. The fitting results show that for the simultaneous SED fit the intrinsic reddening is higher than that claimed for the non-simultaneous fit.

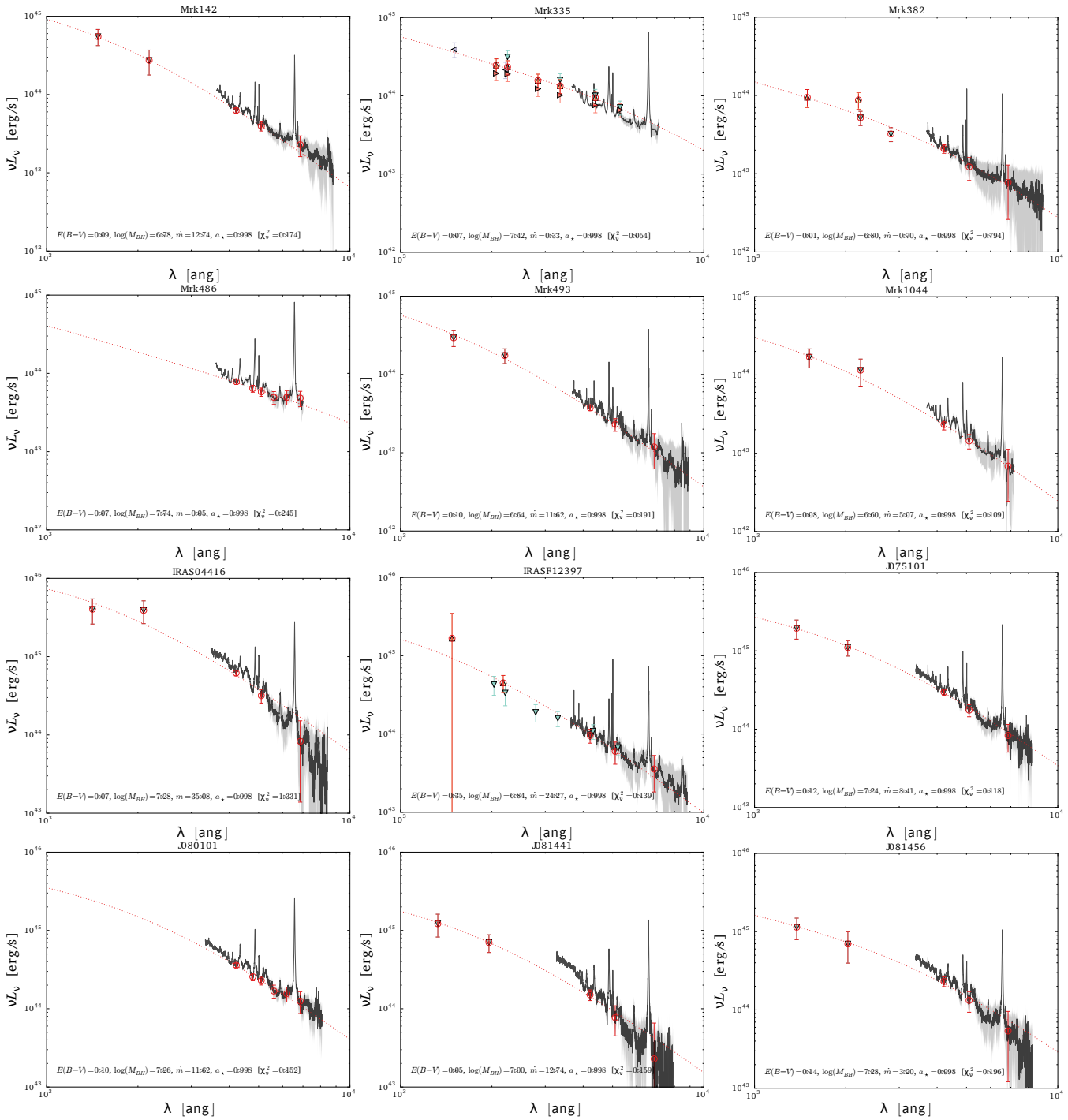

Figure A1. Intrinsic optical-to-UV SED with the best-fit thin AD model over-plotted assuming $a_\star = 0.998$ (red-dotted curves) and $\cos\theta$=0.75. The SED is corrected for Galactic extinction, host-galaxy emission and corrected for intrinsic reddening which was modelled with a classical SMC extinction curve. The order of the objects is the same as in Table A1. Red empty circles represent the continuum regions used for fitting the models to the spectra, and the full points show the available photometric data points: GALEX FUV 1551Å, OM UVW2 2120Å, GALEX NUV 2306Å, OM UVM2 2310Å, OM UVW1 2910Å, OM U 3440Å, OM B 4500Å, OM V 5430Å.

NGC 5548

There is a variability of a factor ∼4 between the OM photometric point at the effective wavelength 5430Å and the optical spectrum. The non-simultaneous dataset (GALEX plus the optical spectrum) was also fitted in order to be compared with the contemporaneous SED given by the OM dataset. Both constructed SED are in good agreement and the best fit in both demand for some dust attenuation.

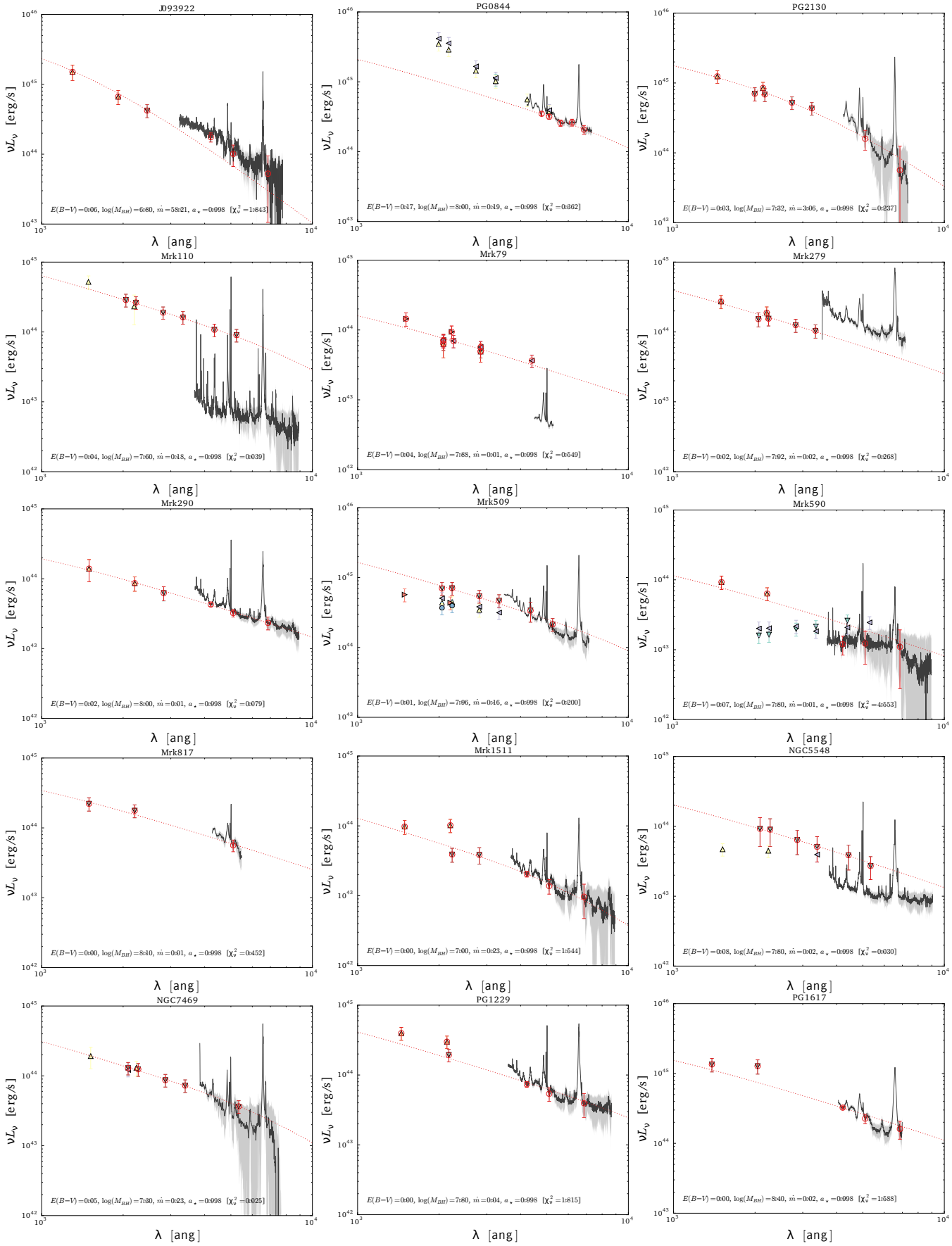

Figure A1. continue . . .

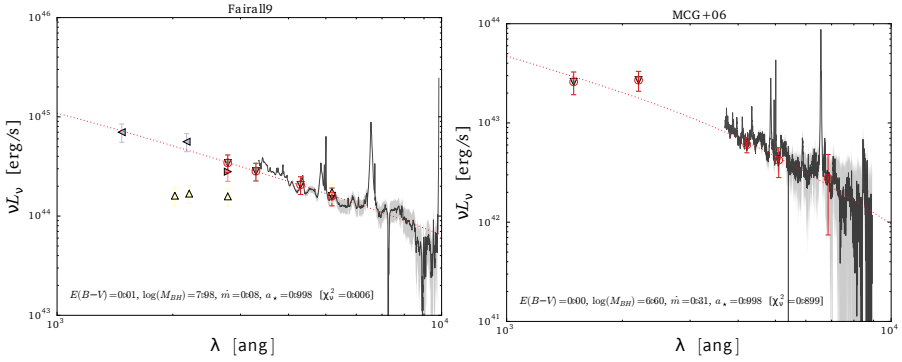

Figure A1. continue

Table B1. Measured and deduced physical parameters

Object	Host Galaxy template	f	THIN AD MODEL A_V	$\log M_{BH}$ $[M_\odot]$	$\log \dot{M}$ $[M_\odot/\mathrm{yr}]$	spin	η	L_{AGN} $10^{44}\mathrm{erg/s}$	$\dot{m}$	χ^2_ν	Dataset
Mrk335	ssp_11Gyr_z05	0.24	$0.15^{+0.07}_{-0.02}$	7.30	-0.85	-1.000	0.038	3.04	0.27	0.556	GALEX+spec
	ssp_11Gyr_z05	0.24	$0.22^{+0.45}_{-0.22}$	7.40	-0.80	0.600	0.091	8.17	0.24	0.044	OM (2000)
	ssp_11Gyr_z05	0.24	$0.34^{+0.41}_{-0.20}$	7.40	-0.65	-0.200	0.052	6.59	0.34	0.014	OM (2007)
	ssp_11Gyr_z05	0.24	$0.37^{+0.28}_{-0.14}$	7.40	-0.75	-0.200	0.052	5.24	0.27	0.121	OM (2009)
IRASF12397	ssp_11Gyr_z05	0.52	$1.63^{+0.26}_{-0.13}$	7.11	0.04	-0.200	0.052	32.37	3.25	0.189	GALEX+spec
	ssp_11Gyr_z05	0.52	$1.89^{+0.00}_{-0.12}$	7.28	0.04	0.000	0.057	35.49	2.22	1.698	OM (2005)
Mrk279	ssp_11Gyr_z02	0.33	$0.06^{+0.17}_{-0.06}$	7.90	-1.60	0.998	0.321	4.57	0.01	0.337	GALEX+OM
	ssp_11Gyr_z02	0.33	$0.00^{+0.33}_{-0.00}$	8.40	-1.65	0.998	0.321	4.07	0.00	0.277	spec
Mrk509	ssp_11Gyr_z02	0.35	$0.03^{+0.06}_{-0.03}$	7.70	-0.85	0.998	0.321	25.69	0.11	0.123	GALEX+spec
	ssp_11Gyr_z02	0.35	$0.21^{+0.11}_{-0.21}$	7.90	-0.45	0.998	0.321	64.52	0.17	0.035	OM (2009)
NGC5548	ssp_11Gyr_z05	0.34	$0.25^{+0.12}_{-0.25}$	8.00	-2.70	0.998	0.321	0.36	0.00	1.324	GALEX+spec
	ssp_11Gyr_z05	0.34	$0.44^{+0.34}_{-0.44}$	8.50	-2.20	0.998	0.321	1.15	0.00	0.070	OM (2013)
NGC7469	ssp_11Gyr_z02	0.70	$0.14^{+0.43}_{-0.14}$	7.10	-1.05	0.600	0.091	4.59	0.27	0.389	GALEX+spec
	ssp_11Gyr_z02	0.70	$0.34^{+0.28}_{-0.25}$	7.70	-1.30	0.600	0.091	2.58	0.04	0.092	OM (2009)

Fairall 9

As has been seen in previous works, the OM observations manifest variability of a factor ∼2.5 at the effective wavelength 2910Å. We decline to the simultaneous SED due to the poor statistic of the contemporaneous OM dataset. The good agreement between the highest OM flux state with the GALEX data makes the non-simultaneous SED the best data to perform our study.

NGC 7469

The contemporaneous photometric points are in good agreement with both the GALEX data and the optical spectrum. The simultaneous SED fit is in good agreement with the non-simultaneous dataset and also require a similar dust extinction correction, being both fits highly consistent.

Mrk 382, J093922, Mrk 290, Mrk 1511, PG 1229

The good agreement between the near-UV GALEX flux with the OM photometric point allow us to use both in conjunction with the optical spectrum as the most convenient approach to model the optical/UV underlying continuum.

Mrk 590

Note that there is a real disagreement between the OM photometry and the optical spectrum. We decide not to use the OM photometry.

This paper has been typeset from a TEX/LATEX file prepared by the author.